

1 **Modern speleothem oxygen isotope hydroclimate records**  
2 **in water-limited SE Australia**

3 <sup>1,2,3,4</sup>Monika Markowska, <sup>2,5</sup>Mark O. Cuthbert, <sup>2,3\*</sup>Andy Baker, <sup>1,2</sup>Pauline C. Treble, <sup>2,6</sup>Martin  
4 S. Andersen, <sup>7</sup>Lewis Adler, <sup>1</sup>Alan Griffiths, <sup>8</sup>Silvia Frisia.

5

6 <sup>1</sup>*ANSTO, Lucas Heights, Sydney 2234, Australia*

7 <sup>2</sup>*Connected Waters Initiative Research Centre, UNSW Australia, Kensington, Sydney 2033,*  
8 *Australia.*

9 <sup>3</sup>*School of Biological, Earth and Environmental Sciences, UNSW Australia, Kensington,*  
10 *Sydney 2033, Australia.*

11 <sup>4</sup>*Faculty of Geosciences, Tübingen University, Tübingen, 72074, Germany*

12 <sup>5</sup>*School of Earth and Ocean Sciences, Cardiff University, Cardiff, CF10 3AT, UK*

13 <sup>6</sup>*School of Civil and Environmental Engineering, UNSW Australia, Kensington, Sydney 2033,*  
14 *Australia.*

15 <sup>7</sup>*Bioanalytical Mass Spectrometry Facility, Mark Wainwright Analytical Centre, UNSW*  
16 *Australia, Kensington, Sydney 2033, Australia.*

17 <sup>8</sup>*School of Environmental and Life Science, University of Newcastle, Callaghan NSW, 2308,*  
18 *Australia.*

19 *\*Corresponding author: a.baker@unsw.edu.au*

20

21 **Keywords:** speleothems, water-limited climate, water isotopes, hydroclimate,

22

23

## 24 **Abstract**

25 Dryland regions are generally projected to become drier under future climate change  
26 scenarios. Understanding the long-term natural variability of dryland regions via paleo-  
27 reconstructions is therefore highly desirable. The  $\delta^{18}\text{O}$  of two coeval modern speleothems  
28 from Cathedral Cave, Wellington, in semi-arid SE Australia are compared to the instrumental  
29 record to assess their efficacy as a proxy of past hydrological variability. Stalagmite  $\delta^{18}\text{O}$  was  
30 found to be modulated by the frequency of recharge events and epikarst evaporation of  
31 storage water. Prolonged intervals between recharge events, such as droughts, resulted in  
32 higher stalagmite  $\delta^{18}\text{O}$ . Conversely, periods with more frequent recharge events and positive  
33 water balance, resulted in lower  $\delta^{18}\text{O}$ . Disequilibrium cave processes are likely to be  
34 enhanced during dry conditions, although it is argued that these will modulate  $\delta^{18}\text{O}_{\text{spel}}$  in the  
35 same direction as epikarst evaporation, effectively amplifying the response of  $\delta^{18}\text{O}_{\text{spel}}$   
36 Extreme events, such as floods and droughts, were also captured in the stalagmite records,  
37 although potentially with a lag of several years. We verify that modern speleothems from  
38 semi-arid regions can be used to reconstruct hydroclimate due to variations in  $\delta^{18}\text{O}_{\text{spel}}$   
39 modulated by karst processes. Such records are archives of past changes in recharge rather  
40 than precipitation amount or surface temperature, as is commonly applied to speleothem  
41 records from non-water-limited regions.

## 42 **1. Introduction**

43 Drylands are water-limited regions where precipitation is less than potential  
44 evapotranspiration, causing either perennial or seasonal soil water deficits (D'Odorico and  
45 Porporato, 2006). They cover approximately 45 % of Earth's land surface and contain  
46 approximately 30% of its population (STAP, 2010). Globally, the largest expansion of  
47 drylands over the last 60 years has occurred in semi-arid regions (Huang et al., 2016). In  
48 Australia, a large portion of the area outside of the central arid desert regions are semi-arid  
49 and dry sub-humid drylands, which are also predicted to expand (Feng and Fu, 2013).  
50 Predicting the hydroclimatic response to climate change on the Australian continent, and  
51 particularly in SE Australia with the densest population, is therefore highly desirable.

52

53 One approach to understanding hydroclimate change is to use proxy records to obtain records  
54 of past hydroclimate variability. Speleothems are a particularly useful proxy in this regard, as  
55 they form directly from subsurface percolation waters (cave drips and seeps) which can  
56 contain geochemical indicators of environmental change (Fairchild and Baker, 2012).  
57 However, our current understanding of speleothem-forming processes is biased to  
58 cave-monitoring in regions with surplus water balances and frequent groundwater recharge.  
59 Significant exceptions are monitoring programs at Soreq Cave, Israel (Bar-Matthews et al.,  
60 1996; Ayalon et al., 1998; Even et al., 1986; Lange et al., 2003; Kaufman et al., 2003); Sif  
61 Cave, Israel (Sheffer et al., 2011); Cathedral Cave, Australia (Cuthbert et al., 2014a, b;  
62 Rutledge et al., 2014; Rau et al., 2015; Rutledge et al., 2015; Markowska et al., 2016;  
63 McDonough et al., 2016; Baker et al., 2016a); and St. Michaels Cave, Gibraltar (Mattey et  
64 al., 2008; Mattey et al., 2010; Mattey et al., 2013; Baker et al., 2014). These studies have  
65 demonstrated that commonly used climate proxies in speleothems, such as  $\delta^{18}\text{O}_{\text{spel}}$ , may have  
66 different interpretations in dryland environments, owing to a higher likelihood of: (1)

67 discontinuous calcite precipitation, (2) non-equilibrium calcite precipitation, (3) high  
68 heterogeneity of karst hydrology, and (4) large soil moisture deficits which must be  
69 overcome to initiate recharge.

70

71 Drip interval and drip water supersaturation are theoretically the primary controls on kinetic  
72 fractionation during calcite precipitation, due to rapid degassing resulting in enhanced  
73 fractionation of the resulting  $\delta^{13}\text{C}_{\text{calcite}}$  and  $\delta^{18}\text{O}_{\text{calcite}}$  (Mühlinghaus et al., 2007, 2009). In  
74 dryland regions, the water-limited environment is a major control on drip hydrology and may  
75 consequently have the largest influence on in-cave isotopic fractionation. The dependence of  
76  $\delta^{18}\text{O}_{\text{calcite}}$  fractionation on drip interval is less than for  $\delta^{13}\text{C}_{\text{calcite}}$ , due to the buffering effects  
77 of the water solution (Mühlinghaus et al., 2009; Scholz et al., 2009). If degassing is  
78 sufficiently rapid, the  $\text{CO}_2$  loss from solution is typically greater than the typical exchange  
79 time of several minutes between  $\text{HCO}_3^-$  and  $\text{H}_2\text{O}$  in solution (Scholz et al., 2009). This results  
80 in kinetic fractionation and higher  $\delta^{13}\text{C}_{\text{calcite}}$  and  $\delta^{18}\text{O}_{\text{calcite}}$  values (Mickler et al., 2006; Baker  
81 et al., 2011). In dryland caves with relatively low relative humidity, in-cave processes may  
82 also play a role in modifying the  $\delta^{18}\text{O}$  in both drip waters and calcite. Deininger and Scholz  
83 (2019) demonstrated theoretically the significance of in-cave evaporation on driving  
84 disequilibrium isotopic fractionation for both  $\delta^{18}\text{O}_{\text{calcite}}$  and  $\delta^{13}\text{C}_{\text{calcite}}$  due to the loss of  $\text{H}_2\text{O}$   
85 from the precipitating solution, which results in an increase in  $\text{Ca}^{2+}_{(\text{aq})}$  concentration, faster  
86 precipitation rates and greater isotopic fractionation.

87

88 Soil and karst hydrology can also be a significant control on the oxygen isotope signature  
89 observed in cave drips and associated speleothems in dryland regions. For example, drip  
90 water  $\delta^{18}\text{O}_{\text{drip}}$  may be higher relative to precipitation  $\delta^{18}\text{O}_{\text{precip.}}$  due to epikarst evaporation. In  
91 studies in Israel and Australia, this isotopic enrichment was observed to be +1.5 ‰ to +3 ‰,

92 respectively (Bar-Matthews et al., 1996; Cuthbert et al., 2014; Markowska et al., 2016). As in  
93 more humid regions, hill-slope aspect can favour evaporative enrichment of subsurface water,  
94 where slopes with greater sun exposure are associated with higher  $\delta^{18}\text{O}_{\text{drip}}$  (Denniston et al.,  
95 1999). The proportion of total precipitation likely to reach subsurface karst may be less in  
96 drylands compared to humid regions, due to larger antecedent soil moisture deficits (Sheffer  
97 et al., 2011; Jex et al., 2012). As a result, recharge  $\delta^{18}\text{O}_{\text{drip}}$  may be biased towards high  
98 magnitude precipitation events. For example, large convective storms are often associated  
99 with lower  $\delta^{18}\text{O}_{\text{precip}}$  values, even in mid-latitude regions (Ayalon et al. 1998; Fleitmann et  
100 al., 2004; Treble et al., 2005). Rayleigh distillation, whereby  $^{18}\text{O}/^{16}\text{O}$  isotopes are fractionated  
101 between liquid and vapour, is enhanced in rapidly ascending air masses, resulting in  
102 precipitation with low  $\delta^{18}\text{O}$  values (Dansgaard, 1964; Rozanski et al., 1993). In a global  
103 analysis of  $\delta^{18}\text{O}_{\text{drip}}$  records, recharge-weighted  $\delta^{18}\text{O}_{\text{precip}}$  was shown to best explain  $\delta^{18}\text{O}_{\text{drip}}$  in  
104 warm climate regions (Baker et al. 2019). Consequently, dryland speleothem  $\delta^{18}\text{O}_{\text{spel}}$  should  
105 be interpreted as a  $\delta^{18}\text{O}_{\text{precip}}$  signal that is potentially highly modified by subsurface  
106 evaporative enrichment and subject to larger recharge thresholds due to low antecedent soil  
107 moisture and high evaporation rates. It may be more valid to consider these records as  
108 reconstructions of recharge frequency/intensity rather than simply mean precipitation  
109  $\delta^{18}\text{O}_{\text{precip}}$  (Markowska et al, 2016; Baker et al., 2019).

110

111 In dryland regions,  $\delta^{18}\text{O}_{\text{drip}}$  is likely to be biased to the isotopic signature of recharge events,  
112 and potentially also the extent of partial evaporation of epikarst water. In addition, cave  
113 environments with low humidity and water supply limitations on drip rates lead to conditions  
114 suitable for the disequilibrium precipitation of calcite are likely, resulting in greater extent of  
115  $\delta^{18}\text{O}_{\text{calcite}}$  fractionation. Also, replication of coeval stalagmites oxygen isotope records may be  
116 lower in dryland caves, which are more water-limited and sensitive to hydrological changes

117 at the individual drip level, compared to caves with well-mixed large water storage reservoirs  
118 from temperate environments. An assessment of the replicability of  $\delta^{18}\text{O}_{\text{spel}}$  and hydroclimate  
119 signal contained in  $\delta^{18}\text{O}_{\text{spel}}$  from a dryland site is required to increase our understanding of  
120 cave processes and investigate the dominant processes impacting the speleothem  $\delta^{18}\text{O}$  record  
121 in water-limited environments. Here, we make such an assessment by comparing two  
122 modern, chronologically-constrained stalagmite  $\delta^{18}\text{O}$  time series to the instrumental record.  
123 The instrumental era (<160 years) provides a critical test period for paleoclimate records  
124 derived from natural archives (Anderson et al., 1998; Matthey et al., 2008; Moquet et al.,  
125 2016). We use an established  $^{14}\text{C}$  bomb-pulse age-model (Markowska et al. 2019) to  
126 constrain the chronology for the two modern (1935-2010 CE) speleothems from Cathedral  
127 Cave, SE Australia. A previously-developed karst hydrological model for the site (Cuthbert  
128 et al., 2014a) is extended for the period of speleothem deposition to model speleothem  
129  $\delta^{18}\text{O}_{\text{spel}}$ . This model uses an evaporative enrichment function to assess whether the variability  
130 in  $\delta^{18}\text{O}_{\text{spel}}$  can be explained by karst hydrology and the extent to which a climate signal is  
131 preserved in the stalagmite. The implications of these results for the identification of suitable  
132 speleothems for hydroclimate reconstruction in water-limited environments are addressed.

133

## 134 **2. Background**

### 135 **2.1 Cave environment**

136 Cathedral Cave is located at Wellington Caves Reserve, New South Wales, Australia  
137 ( $32^{\circ} 37'S$ ;  $148^{\circ} 56'E$ ) (Figure 1, cave map: Figure S1). The cave descends to approximately  
138 30 m below land surface and has formed within Devonian limestone which has been  
139 marmorised, leaving no primary porosity. Water flow is dominated by fracture-flow. A thin-  
140 layer of red-brown soil comprising clays, iron oxides, fine quartz sands, and calcite nodules,

141 with aeolian contributions, overlies the limestone (Baker et al., 2016a). Soil cover is not  
142 complete, with exposed karstified limestone abundant. Where present, soil thickness is  
143 typically less than 20 cm, with a thin (< 5 cm) organic layer followed by a sandy-clay  
144 textured soil down to bedrock (Berthelin et al. 2019). Cathedral Cave is within a temperate  
145 semi-arid region, with mean annual precipitation of 619 mm (1956-2005 CE) and pan  
146 evaporation of 1825 mm (1956-2005 CE) recorded 7 km north of the cave at Wellington  
147 (Bureau of Meteorology, 2015; climate data accessible at [www.bom.gov.au/climate/data/](http://www.bom.gov.au/climate/data/)).  
148 There is a large seasonal temperature variation, with monthly mean maximum ranging from  
149 15 °C in July and 32 °C in January. Cathedral Cave is a long-term monitoring site for the  
150 modern monitoring of cave drip water hydrology in a water-limited environment. The  
151 stalagmites studied here come from South Passage, at approximately 25 m below land  
152 surface, and within the long-term drip water monitoring network (Jex et al 2012; Cuthbert et  
153 al 2014a).

154

155 Inactive speleothems are apparent throughout Cathedral Cave. Dripping is intermittent in the  
156 upper, drier chambers of the cave and speleothem formation is rare here, whilst speleothem  
157 formation dominates the deeper and wetter ‘South Passage’ where the stalagmites in this  
158 study were collected. South Passage generally has high relative humidity ( $97.1 \pm 0.7\%$ ; Rau  
159 et al., 2015), little evidence of in-cave evaporative enrichment of water from evaporative pan  
160 experiments ( $<0.1 \text{ ‰} / \text{h}$ ,  $\delta^{18}\text{O}_{\text{water}}$ ) (Markowska et al., 2016), and high cave air  $\text{CO}_2$  (mean  
161 concentration: 3535 ppm in winter, 7784 ppm in summer; McDonough et al., 2016).  $\delta^{18}\text{O}_{\text{drip}}$   
162 is dominated by evaporation of stored karst water under high humidity (Cuthbert et al.,  
163 2014a). During periods of low recharge,  $\delta^{18}\text{O}_{\text{drip}}$  typically has more positive values (Cuthbert  
164 et al., 2014a; Markowska et al., 2016).

165

## 166 **2.2 Wellington Caves climate, 1930 to 2010 CE**

167 Figure 2 shows the temperature anomaly ( $^{\circ}\text{C}$ ), deep drainage (mm / d), monthly potential  
168 evaporation (mm) and annual rainfall amount (mm / a). At Wellington, mean annual  
169 temperature over 1900-2014 CE is  $16.7^{\circ}\text{C}$  (Raupach et al. 2009, 2012; Figure 2). Overnight  
170 minimum temperature has increased by  $+0.4^{\circ}\text{C}$  since approximately 1950 CE (Figure 2),  
171 consistent with observations across the Australian continent in general (Fawcett et al., 2012;  
172 Trewin, 2013). The monthly Cumulative Rainfall Departure (CRD) and seasonal CRD, were  
173 calculated based on the cumulative departures from the mean monthly rainfall over the  
174 speleothem growth period 1930-2010 CE (Weber and Stewart, 2004; Bredenkamp, 1995).  
175 This approach is based on the principle that the cumulative departures from mean rainfall  
176 should broadly reflect changes in groundwater levels (eg. Butterworth et al., 1999). Monthly  
177 mean rainfall shows weak seasonality and large inter-annual variability (Markowska et al.,  
178 2016), associated with four major climate phenomena (El Niño Southern Oscillation (ENSO),  
179 Indian Ocean Dipole (IOD), Southern Annular Mode (SAM) and the Interdecadal Pacific  
180 Oscillation (IPO) (Pittock et al., 2006; Verdon-Kidd and Kiem, 2009; Ummenhofer et al.,  
181 2011; Christensen et al. 2013; King et al., 2013).

182

183 Climate predictions for SE Australia suggest further pressure on water resources, due to (1)  
184 anticipated decreases in cool season precipitation due to poleward expansion of the  
185 subtropical dry zone (Christensen et al., 2013) and decreasing groundwater recharge in  
186 (Crosbie et al., 2013), coupled with a global increase in drought frequency and/or severity  
187 (Dai, 2013). However, the general trend of declining rainfall over SE Australia during the  
188 latter half of the 20<sup>th</sup> Century reported by others (Nicholls, 2010; BoM, 2015) is not  
189 represented in annual rainfall totals at Wellington. Seasonal cumulative rainfall departure  
190 time-series exhibit contrasting seasonal trends, with increasing spring rainfall and decreasing



191 winter rainfall since 1960 CE. The latter has likely exacerbated the reduction in recharge,  
192 since infiltration of cool season rainfall tends to be more hydrologically effective due to  
193 lower potential evapotranspiration (PET) and higher soil moisture saturation. Two periods of  
194 deep drainage (defined as when water drains from the bottom of the modelled deep soil layer  
195 (6 m) into the groundwater stores) occur during the 1950's and early 1990's (Raupach et al.,  
196 2009, 2012; Figure 2).

197

198 Potential evaporation (PE) is derived using solar irradiance data from satellite imagery from  
199 1990 to present, and for the period 1900-1990 is obtained by using the calibration against  
200 monthly climatological data for the post 1990 CE period. Mean and standard deviation PE is  
201 the same for both time periods (pre-1990: mean = 4.06 mm / day (3.94 - 4.18 95% CI,  
202 n=1080); post-1990: mean = 4.12 mm / day (3.88 to 4.37 95% CI, n = 290). A small decrease  
203 in PE variance (~5%, variance decreases from 4.4 to 4.2 mm / day) is observed in the time  
204 series prior to 1990 CE which is likely to be a calibration artefact. Most recently, the mid-  
205 2000's was correlated with years of persistently declining rainfall. This period, termed the  
206 "Millennium Drought" beginning in 1997 CE (Figure 2), experienced prolonged rainfall  
207 deficits brought about by widespread protracted dry conditions over most of continental  
208 Australia. The drought ended in 2010 CE, after ENSO activity switched to a strong La Niña  
209 phase. This brought about high precipitation resulting in large-scale flooding in many parts of  
210 southeast Australia and east Australia, including the town of Wellington in December 2010  
211 CE (van Dijk et al., 2013). It was the second wettest December on record for the Murray-  
212 Darling Basin region, and Australia's wettest July to December period on record (NCC and  
213 BoM, 2011).

214

215 Drought conditions also occurred in the late 1940's (Figure 2), clearly seen in the sum of  
216 departures in mean monthly rainfall amounts (CRD; Figure 2). This  
217 "WWII Drought", which was widespread over eastern Australia during 1937 – 1945 CE  
218 (Ummenhofer et al., 2009), impacted summer and autumn rainfall totals most. This was  
219 followed by significantly wet conditions in the 1950's, including the highest annual rainfall  
220 on record and the largest flood on record delivering ~180 mm rainfall in 24 hours, flooding  
221 the local town of Wellington (~8 km from the study site) in 1955 CE. This coincided with a  
222 moderate La Niña, which had a strong effect across the eastern third of Australia (BoM,  
223 2010).

224

### 225 **2.3 Stalagmites WB and WC: morphology, chronology and drip regimes**

226 The two stalagmites from Cathedral Cave, "WB" and "WC", were collected in mid-2010 CE  
227 from South Passage and were located approximately 5 m distance from each other. WB grew  
228 over a Bakelite (early plastic) cable installed in 1932 CE, the installation of which likely  
229 resulting in damage to the stalactite tip which re-invigorated dripping. Photographs of the  
230 sectioned samples are presented in Figure 3. WB and WC mostly consist of columnar calcite.  
231 The fabric of WB is more typically open columnar to microcrystalline types (Frisia, 2015),  
232 whereas WC is predominantly composed of compact columnar. In addition, WB appears to  
233 have been characterized by an initial overall greater porosity, which allowed destruction of  
234 the inter-crystalline porosity by early diagenetic cement precipitation (translucent calcite in  
235 Fig. 3A).

236

237 Carbonate  $^{14}\text{C}_{\text{spel}}$  analysis results for stalagmites WB and WC were presented in Markowska  
238 et al (2019). Markowska et al. (2019) constructed an age model for each stalagmite which  
239 produced chronologies that cover the periods from  $1936.7 \pm 3.9$  CE (WB) and  $1982 \pm 2.65$

240 CE (WC) to the date of sampling. The resultant annual deposition rate is greater than 0.2 mm  
241 / year, and for WC over 0.7 mm / year, permitting high temporal resolution  $\delta^{18}\text{O}_{\text{speil}}$  sampling  
242 (see section 3.1).

243

244 The median drip rate for seven other monitored drip sites in South Passage, where WB and  
245 WC were located, is slow, between 0 and 0.2 drips / min (Cuthbert et al., 2014a). The drip  
246 above the site of WC is also slow, with an average drip rate of 0.24 drips / min, slowing to 0  
247 to 0.02 drips / min during non-recharge periods and up to 0.67 drips / min during recharge  
248 periods. No drip data was collected for WB due to insufficient drip height for drip logger  
249 installation; however, opportunistic observations suggest that WB had an overall faster drip  
250 rate than WC. In addition, during field observations in January 2016 CE the drip above WC  
251 was dry, but the drip above WB was still active – suggesting that stalagmite WB had access to  
252 a larger karst water reservoir. Prior to January 2016 CE, the last rainfall event to significantly  
253 increase drip discharge in South Passage, and by inference increase the volume of water in  
254 the overlying stores, was in July 2013 CE (see Markowska et al 2016, Fig 2).

255

## 256 **3 Methods**

### 257 **3.1 Carbonate $\delta^{18}\text{O}$ and $\delta^{13}\text{C}$ analysis**

258 Slices 13 mm and 6 mm thick were cut from the central growth axis of stalagmites WB and  
259 WC respectively and then halved along the growth axis, on the right-hand side edge of an  
260 apparent dissolution hole in order to maximize sample recovery (Panel C, Figure 3). A  
261 Micromill 2000 ER-LR system with mechanical repeatability (precision) of 0.0127 mm was  
262 used to obtain sample powders. Carbonate powders were milled continuously from each  
263 stalagmite, using a 2 mm diameter tungsten carbide drill bit, along the edge of the growth  
264 axis in 0.1 mm increments (x-axis), 2 mm (y-axis) and 2 mm (z-axis) (WC, n = 220 and WB,

265 n = 360). Milling transects for isotopic analysis are shown in Figure 3, Panels C and D.  
266 Approximately 20-40  $\mu\text{g}$  sub-samples of these powders were analysed on the MAT-253  
267 Isotope Ratio Mass Spectrometer with Kiel carbonate device (Thermo Fisher Scientific,  
268 Bremen, Germany) at the Mark Wainwright Analytical Centre at UNSW Australia. They  
269 were reacted at 70 °C with 2 drops of 100 % phosphoric acid. The Kiel IV carbonate device  
270 settings used were a reaction one time of 420 s, a reaction two time of 120 s and a transfer  
271 time of 90 s. An integration time of 16 s and 8 cycles was used for the isotopic measurement  
272 of  $\text{CO}_2$  gas. Data were standardized to the Vienna Pee Dee Belemnite (VPDB) scale using  
273 IAEA National Bureau Standards NBS-18 ( $\delta^{18}\text{O} = -23.20 \text{ ‰}$  and  $\delta^{13}\text{C} = -5.01 \text{ ‰}$ ) and NBS-  
274 19 ( $\delta^{18}\text{O} = -2.20 \text{ ‰}$  and  $\delta^{13}\text{C} = +1.95 \text{ ‰}$ ) using a two-point calibration. The analytical  
275 precision of the standards calculated for these datasets was 0.05 ‰ and 0.06 ‰, for  $\delta^{13}\text{C}$  and  
276  $\delta^{18}\text{O}$ , respectively.

277

### 278 **3.2 Karst hydrology $\delta^{18}\text{O}$ model**

279  $\delta^{18}\text{O}_{\text{spel}}$  is modelled using a Soil Moisture Balance (SMB) model first presented in Cuthbert  
280 et al. (2013), coupled with a karst hydrology model (Cuthbert et al., 2014a) to simulate  
281 groundwater recharge, shallow karst flow, and oxygen isotopic composition of drip waters.  
282 The combined SMB-karst model was parameterised for Cathedral Cave and successfully used  
283 to model drip water isotopic composition for a range of drips from South Passage for  
284 monthly-integrated samples (Markowska et al., 2016) over a two-year period in Cuthbert et  
285 al. (2014a). Unique to the study of Cuthbert et al (2014a) was a function to model the isotopic  
286 evolution of drip waters due to epikarst evaporation under high humidity conditions  
287 following Gonfiantini (1986). This accounted for the measured  $^{18}\text{O}$  enrichment of karst drip  
288 waters relative to rainfall  $^{18}\text{O}$ , which fell on the local meteoric waterline rather than an

289 evaporation line typical of water evaporated under low humidity (Cuthbert et al., 2014a). The  
290 sensitivity of all model parameters was assessed in Cuthbert et a (2014a). The model  
291 structure (Figure S2) and code are available in the Supplemental Materials.

292

293 Here, the model is extended back through the 20<sup>th</sup> century, keeping the same parameters as  
294 previously calibrated for the SMB-karst model. For the isotope model, since the previous  
295 calibration was carried out for a wide range of drips, a slight modification was needed for the  
296 parameters to best represent the drip feeding WB. Based on field observations (see section 2),  
297 WB had a relatively faster drip rate compared with the range of drips previously represented  
298 in the model. It was assumed from this higher drip rate, that WB is fed by a larger store.  
299 Hence, the parameter S2Lim (the depth in the modelled box karst reservoir where epikarst  
300 evaporation ‘turns on’) was decreased from 60 mm to 20 mm, to reduce the level at which  
301 evaporation became important. In the parameterisation of this model, perhaps  
302 counterintuitively, a higher S2Lim parameter (greater depth) results in higher evaporation  
303 due to the greater range of depths where the evaporation term is ‘turned on’, 0-60 mm  
304 opposed to 0-20 mm. The epikarst evaporation rate was also reduced from 0.04 mm / d to  
305 0.01 mm / d in order to capture an oxygen isotopic composition closer to mean rainfall.

306

307 Precipitation-weighted mean annual rainfall ( $\delta^{18}\text{O}_{\text{precip}} = \sim -4 \text{ ‰}$ ) was used as the model input,  
308 based on two years of rainfall monitoring (Cuthbert et al., 2014a). This value is close to  
309 modern groundwater values (mean = -4.78 ‰, n = 11) from Spicers Creek catchment 68 km  
310 away (Morgan et al., 2006) and at in two boreholes at Wellington Caves that were monthly  
311 sampled between November 2013 and July 2014 (BH1:  $-4.28 \pm 0.29 \text{ ‰}$ ; BHGolf:  $-4.70 \pm$   
312  $0.20 \text{ ‰}$ ; Keshavarzi, 2018). Monthly-integrated  $\delta^{18}\text{O}_{\text{precip}}$  presented in Cuthbert et al. (2014)  
313 over the two-year monitoring period has a very weak relationship with rainfall amount ( $r^2 =$

314 0.03;  $p > 0.05$   $n = 24$ ). However, end member event isotopic rainfall composition of  $< 5$  mm  
315 and  $> 45$  mm suggests there may be a stronger relationship if event-based samples are  
316 considered (Figure 4, Supplementary Figure 2). Opportunistic rainfall event samples (0.5 - 24  
317 h), sporadically collected over 2010 - 2012 CE (data available as Supplemental Materials).  
318 Samples were stored in glass bottles with no headspace and analysed on the Los Gatos ©  
319 cavity ring down mass spectrometer at UNSW Australia. The overall precision was  $\pm 0.12$  ‰  
320  $\delta^{18}\text{O}$  and  $\pm 1.2$  ‰  $\delta\text{D}$ . Event end-member samples showed a moderate  $\delta^{18}\text{O}_{\text{precip}}$  relationship  
321 with daily rainfall amount ( $r^2 = 0.48$ ;  $p < 0.05$ ,  $n = 12$ ) (Figure S3). This correlation was  
322 considered too weak to be used as a transfer function to enable a calculated rainfall  $\delta^{18}\text{O}_{\text{precip}}$   
323 time series to be used as the model input. However, as a test of how the model might perform  
324 if such an input was known, a value of  $\delta^{18}\text{O}_{\text{precip}} = -12$  ‰ was used as the input value for the  
325 most extreme rainfall events ( $>120$  mm / d) observed at this site based on event rainfall  
326 samples (e.g.  $\delta^{18}\text{O}_{\text{precip}} = -11.3$  ‰ after  $\sim 105$  mm rainfall over two days). All other  
327 parameterisation was the same as in Cuthbert et al. (2014a).

328

329 Since the original model was calibrated for drip water oxygen isotopes, a correction was  
330 required to convert the modelled data ( $\delta^{18}\text{O}_{\text{drip}}$  VSMOW) to a calcite equivalent ( $\delta^{18}\text{O}_{\text{calcite}}$   
331 VPDB) for comparison with the measured  $\delta^{18}\text{O}_{\text{spel}}$ . This conversion was based on a  $\text{CO}_2\text{-H}_2\text{O}$   
332 fractionation factor of 1.0412, an acid fractionation factor for  $\text{H}_3\text{PO}_4$  liberated  $\text{CO}_2$  from  
333 calcite of 1.01025 (Freidman and O'Neil, 1977), and a  $\text{H}_3\text{PO}_4$ -liberated  $\text{CO}_2$  from VPDB-  
334  $\text{CO}_2$  in equilibrium with VSMOW of 1.00027 (Gonfiantini, 1984; Hut, 1987) following  
335 Coplen (1988), Eq. 12, (p. 295). The in-cave temperature dependent fractionation at the time  
336 of calcite precipitation from drip water was calculated from the equation of Kim and O'Neil  
337 (1997) and the mean annual surface temperatures from the AWAP database (Raupach et al.,  
338 2009, 2012) to produce predicted calcite  $\delta^{18}\text{O}_{\text{calcite}}$ . It is assumed that evaporative cooling is

339 negligible at the stalagmite sites of WB and WC in South Passage, as the RH is ~97% most  
340 of the time (Rau et al., 2015)

341

## 342 **4 Results**

### 343 **4.1 Stalagmite $\delta^{18}\text{O}$ time series**

344 Time series and  $\delta^{18}\text{O}_{\text{spel}}$  vs.  $\delta^{13}\text{C}_{\text{spel}}$  scatterplots for stalagmites WB and WC are compared in  
345 Figure 5. The isotopic time series for WB is seasonally resolved (~4.9 samples / year) and for  
346 WC is bi-monthly resolved (~7.9 samples / year). The isotopic mean of WC is offset overall  
347 by approximately +0.5 ‰ ( $\delta^{18}\text{O}_{\text{spel}}$ ) and +1.2 ‰ ( $\delta^{13}\text{C}_{\text{spel}}$ ) relative to WB (Figure 5), and by  
348 +0.3 ‰ ( $\delta^{18}\text{O}_{\text{spel}}$ ) and +1.4 ‰ ( $\delta^{13}\text{C}_{\text{spel}}$ ) over the period of overlapping growth. Both  
349 stalagmites have  $\delta^{18}\text{O}_{\text{spel}}$  approximately 1 ‰, higher than the precipitation-weighted mean  
350 annual rainfall when rainfall is considered on the equivalent (VPDB) scale, i.e. mean rainfall  
351 of -4 ‰ VSMOW should theoretically form calcite with  $\delta^{18}\text{O}$  of -4.9 ‰ using the equation  
352 from Kim and O'Neil (1997).

353

354 The two stalagmite records overlap from  $1982 \pm 2.65$  CE onwards. With respect to mean  
355  $\delta^{18}\text{O}_{\text{spel}}$ , the comparison between the two stalagmite records between 1990 and 2004 CE is  
356 typically within 0.5 ‰ (Figure 6). Both  $\delta^{18}\text{O}$  records show sub-decadal and longer-term  
357 trends throughout their respective growth periods, but there is typically less variability in WB  
358 which appears more smoothed relative to WC (Figure 5).

359

360 Comparing the sub-decadal trends and peaks, between 1982 and 1990 CE, there is little  
361 agreement between stalagmites, with  $\delta^{18}\text{O}_{\text{spel}}$  maxima in 1985 and 1987 CE in WC not  
362 represented in WB. Starting in 1990 CE,  $\delta^{18}\text{O}_{\text{spel}}$  becomes more positive in both stalagmites

363 by ~1 ‰ for about 5 years, followed by a ~1 ‰ decrease until 2000 CE. Following this,  
364  $\delta^{18}\text{O}_{\text{spel}}$  of both stalagmites begins to increase again by ~1.2 ‰, with maximum values  
365 around 2002 and 2003 CE (Figure 5). The subsequent decrease in  $\delta^{18}\text{O}_{\text{spel}}$  was greatest in WB  
366 (1 ‰) compared to WC (0.4 ‰). After this minima,  $\delta^{18}\text{O}_{\text{spel}}$  for both stalagmites increased by  
367 +1.4 ‰ up to 2010 CE. This was a smooth  $\delta^{18}\text{O}_{\text{spel}}$  increase in WB, whereas in WC the  
368 general increasing trend was punctuated by peaks and troughs in  $\delta^{18}\text{O}_{\text{spel}}$  every 1 - 2 years  
369 (Figure 5). We statistically compared the correlation between the two stalagmites for the post  
370 1990 CE period, after interpolating the  $\delta^{18}\text{O}_{\text{spel}}$  series to a common timescale, normalising to  
371 z values, and detrending (0.05 z-score /yr), and then investigated all correlations within the  
372 chronological uncertainties of the two stalagmites. Despite the visual correlations, the  
373 maximum Kendall's Tau value was 0.21, confirming differences in the number, and  
374 amplitude of, isotope peaks and troughs between the stalagmites.

375

376 Considering the long-term WB  $\delta^{18}\text{O}_{\text{spel}}$  record,  $\delta^{18}\text{O}_{\text{spel}}$  begins at -5.4 ‰ in 1936 CE and  
377 increases to -3.3 ‰ by 1948 CE, punctuated by a short-term trough in 1947 CE (Figure 5).  
378 WB  $\delta^{18}\text{O}_{\text{spel}}$  decreases to -5.0 ‰ at 1950 CE. A further increase and decrease of ~1 ‰  
379 occurs, before an increase to -2.5 ‰, the highest value in the WB time series, in 1953 CE.  
380 The lowest value in the record (-6.4 ‰) occurs shortly after (1956 CE), a 4 ‰ decline in  
381 three years. This is accompanied by a slower growth rate (0.12 mm / a) continuing until 1965  
382 CE, where WB  $\delta^{18}\text{O}_{\text{spel}}$  increases to -3.1 ‰ in 1966 CE, although values are ~1 ‰ lower in  
383 the early 1960's.  $\delta^{18}\text{O}_{\text{spel}}$  decreases by ~1 ‰ again until 1970 CE, after which it remains  
384 stable at the long-term  $\delta^{18}\text{O}_{\text{spel}}$  isotopic mean of -4.1 ‰ until the early 1980's.

385

386 **4.1.1 Stalagmite  $\delta^{18}\text{O}$  vs  $\delta^{13}\text{C}$**



387 The  $\delta^{18}\text{O}$  vs  $\delta^{13}\text{C}$  relationship for WC is strong as shown in the scatterplot inset in Figure 5  
388 ( $r^2 = 0.77$ ), suggesting that WC may have precipitated under enhanced disequilibrium  
389 conditions (Desmarchelier et al., 2000). Conversely, WB shows no relationship between  $\delta^{18}\text{O}$   
390 and  $\delta^{13}\text{C}$  ( $r^2 = 0.00$ ), as judged by the scatterplot in Figure 5. This agrees with the observed  
391 speleothem fabrics where WB is more typically open columnar to microcrystalline types,  
392 whereas WC is predominantly composed of compact columnar. Frisia et al. (2018) propose  
393 that cave calcite grows by nanocrystal aggregation rather than classical mechanisms; compact  
394 crystals aggregate and then coalesce, whereas more porous, nanocrystals are bridged by  
395 organics. The compact columnar calcite of WC is due to the slow drip rate, with drip water  
396 having time to degas on the speleothem surface, and with calcite precipitated without much  
397 disturbance by colloidal and particulate matter. In contrast, WB has more open and  
398 microcrystalline fabrics, which can be indicative of the presence of dissolved organic matter  
399 and more disturbance by colloidal and particulate matter. These are representative of a  
400 quicker hydrological connectivity to the surface, agree with the observation of a faster drip  
401 rate, and less disequilibrium calcite deposition from the film of fluid (Dreybrodt and Scholz,  
402 2011; Deininger et al 2012).

403

#### 404 ***4.1.2 $\delta^{18}\text{O}$ relationship with the instrumental climate record***

405 Figure 6 shows the two  $\delta^{18}\text{O}_{\text{spel}}$  records (Panel E) alongside variables: deep drainage (mm / d;  
406 Panel E), water excess (mm / d; Panel D), annual CRD, winter CRD, PE (mm / d; Panel C),  
407 Southern Oscillation Index (SOI; Panel B) anomalies and IOD events (Panel A).  $\delta^{18}\text{O}_{\text{spel}}$   
408 trends are broadly anti-correlated to the monthly CRD (Figure 6). For example, a long-term  
409 15-year decline in the CRD over 1935-1950 CE, an indicator of groundwater levels, is  
410 mirrored by an overall increase in  $\delta^{18}\text{O}_{\text{spel}}$ . Water balance deficits ( $P < ET$ ) also occurred in

411 12 of the 15 years (Figure 6) and the period 1937-1945 CE was recognised as a drought due  
412 to high water deficits (WWII Drought; Figure 6). WC  $\delta^{18}\text{O}_{\text{spel}}$  values are also higher during  
413 drought periods (i.e. Millennium Drought; Figure 6) and show a continuous positive trend,  
414 for example from -4.1 ‰ in 1999 CE to -2.4 ‰ in 2008 CE (Figure 6). In addition, during the  
415 same period, six periodic oscillations in WC  $\delta^{18}\text{O}_{\text{spel}}$  were observed, approximately 1 ‰ in  
416 amplitude and approximately 1 - 2 years in wavelength (numbered 1 to 6; Figure 6). These  
417 correspond with the longest (six consecutive years) period of annual water deficit ( $P < ET$ )  
418 (numbered 1 to 6; Figure 6). The oscillations in the stalagmite do not all occur synchronously  
419 with the climate record, but are within chronological error  $\pm 2.65$  years. This asynchrony  
420 could be due to the uncertainty in the chronology because of non-linear growth or a non-  
421 linear transfer function of surface hydroclimate dynamics to the stalagmite. WB  $\delta^{18}\text{O}_{\text{spel}}$   
422 values in the Millennium Drought were also higher but not dissimilar from other dry (but not  
423 drought) periods in the time series (e.g. 1995-1996 CE) although  $\delta^{18}\text{O}_{\text{spel}}$  did persist above  
424 the arithmetic mean for most of the 2000's (Figure 5).

425

426 Conversely, during periods of water excess ( $P > ET$ ), lower  $\delta^{18}\text{O}_{\text{spel}}$  is typically observed  
427 (Figure 6). For example, in 1950 CE Wellington experienced the highest rainfall year on  
428 record (1386 mm / a), resulting in an estimated deep drainage of ~0.45 mm / d (deep drainage  
429 from AWAP data; Figure 6) and water excess ( $P - ET$  from AWAP data; Figure 6),  
430 coinciding with a trough in  $\delta^{18}\text{O}_{\text{spel}}$ . During periods of high and sustained water excess, e.g.  
431 1969-1974 CE (Figure 6),  $\delta^{18}\text{O}_{\text{spel}}$  is less variable and is similar to arithmetic mean  $\delta^{18}\text{O}_{\text{spel}}$   
432 values (Figure 5).

433

434 A major flood event (1955 CE) is the only part of the WB  $\delta^{18}\text{O}$  time series outside of the  
435 range of observed drip  $\delta^{18}\text{O}_{\text{water}}$  (e.g. -6.4 ‰ VPDB; Figure 5). In the historical record,

436 flooding occurred in the town of Wellington in February 1955 CE due to a trough bringing in  
437 moist airflow associated with a monsoon depression moving down from Queensland  
438 (Australian Bureau of Statistics, 2008), delivering 178 mm of rainfall in 24 hours and ~240  
439 mm over a four-day period. The resulting February 1955 CE rainfall was the highest on  
440 record (BoM, 2010). This flooded the Wellington township and surrounding regional areas  
441 bringing unprecedented rainfall to an area which, in decades previous, had been in drought  
442 conditions (Thorpe and Tweedie, 1956; Walker, 2010). Rainfall event samples over 2011-13  
443 CE (Figure 5) at Wellington revealed that modern  $\delta^{18}\text{O}_{\text{precip}}$  of extreme rainfall events are  
444 likely to be isotopically depleted (e.g. -11.4 ‰ VSMOW, ~105 mm rainfall). The flood  
445 period is a clear outlier in  $\delta^{18}\text{O}_{\text{spel}}$ , with rapid depletion starting in 1955 CE and continuing to  
446 1957 CE (Figure 6). The timing of the surface flood event and rapid  $\delta^{18}\text{O}_{\text{spel}}$  change occur  
447 almost synchronously (Figure 6), suggesting that the karst hydrological response to these  
448 types of events has no measurable lag, although their persistence in the  $\delta^{18}\text{O}$  record continues  
449 years after the flood occurred (e.g. 1956-57 CE) demonstrating the vadose zone hydrologic  
450 memory.

451

## 452 **5 Discussion**

### 453 **5.1 Climatic controls on stalagmite $\delta^{18}\text{O}$**

454 The frequency of effective recharge and partial evaporation of water stored in the karst  
455 control the drip  $\delta^{18}\text{O}_{\text{drip}}$  variability at Cathedral Cave (Cuthbert et al., 2014a; Markowska et  
456 al., 2016). Drip water monitoring has demonstrated that the process of epikarst evaporation  
457 drives the isotopic composition of storage water towards higher values during dry periods.  
458 When recharge occurs, this dilutes the high  $^{18}\text{O}$  storage water with low  $^{18}\text{O}$  from rainfall  
459 events that generate recharge (Cuthbert et al 2014a). With no seasonality in precipitation at

460 the site, annual cycles of depletion and enrichment in  $^{18}\text{O}_{\text{drip}}$  of sampled drips have not been  
461 observed. Furthermore, there is no correlation between monthly rainfall amount and monthly  
462  $\delta^{18}\text{O}_{\text{drip}}$  composition (Markowska et al., 2016).

463

464 The irregular timing of recharge events explains an absence of regular, annual  $\delta^{18}\text{O}_{\text{spel}}$  cycles  
465 in the stalagmite time series (Figure 5). The irregular timing of recharge events means that  
466 variability in  $\delta^{18}\text{O}_{\text{spel}}$  due to intra-annual changes in  $\delta^{18}\text{O}_{\text{precip}}$  will not be uniform (i.e. varying  
467 on a seasonal basis) and are more likely synoptically driven depending on moisture source of  
468 individual rainfall events. Monthly  $\delta^{18}\text{O}_{\text{drip}}$  data suggest that epikarst evaporation could be  
469 responsible for the magnitude of the high frequency increases in  $\delta^{18}\text{O}_{\text{spel}}$ , with shifts in  
470  $\delta^{18}\text{O}_{\text{drip}}$  of up to  $\sim 2\text{‰}$  in the space of several months (Cuthbert et al 2014a). Over the 3-year  
471 drip water monitoring period (2010-2013 CE) drip waters in South Passage varied by  $2.8\text{‰}$   
472 ( $n = 85$ ) with a standard deviation of  $0.45\text{‰}$  (Cuthbert et al 2014a). Observed  $\delta^{18}\text{O}_{\text{spel}}$   
473 variability is all within the same range of observed  $\delta^{18}\text{O}_{\text{drip}}$  (once converted to the equivalent  
474 VPDB scale using the temperature dependent fractionation equations of Kim and O'Neill  
475 (1997)). One exception is the 1955 CE flood period discussed in section 4.2.3. With limited  
476 recharge,  $\delta^{18}\text{O}_{\text{spel}}$  increases from  $-5.0\text{‰}$  to  $-4.2\text{‰}$  (Figure 6) over the WWII drought in  
477 1937-1945 CE. Conversely, recharge causes  $\delta^{18}\text{O}_{\text{spel}}$  to move towards lower values. For  
478 example,  $\delta^{18}\text{O}_{\text{spel}}$  shifted from  $-3.3\text{‰}$  in previously dry years to  $-4.9\text{‰}$ , a difference of  
479  $\sim 1.5\text{‰}$ , after very high precipitation amount in 1950 CE (Figure 6). Overall,  $\delta^{18}\text{O}_{\text{spel}}$  data  
480 supports the previous conclusions in Cuthbert et al. (2014a) from drip monitoring studies in  
481 Cathedral Cave where epikarst evaporation isotopically enriches storage water during dry  
482 periods, punctuated by recharge during wet periods which dilutes high  $^{18}\text{O}$  storage water with  
483 low  $^{18}\text{O}$  water from recharge.

484

## 485 **5.2 Mechanisms affecting speleothem $\delta^{18}\text{O}$ composition**

### 486 **5.2.1 Cave climate**

487 High humidity at the end of the South Passage chamber >97 % (Rau et al., 2015) means both  
488 stalagmites would have experienced a similar cave air environment. Limited ventilation  
489 occurs, with the absence of noticeable airflow, with a measurable decrease in  $\text{CO}_2$  from an  
490 average of 7784 ppm in summer to 3535 ppm in winter (McDonough et al., 2016). As both  
491 stalagmites are at least seasonally resolved, one would expect to see any seasonal changes in  
492  $\delta^{18}\text{O}_{\text{spel}}$  driven by cave ventilation effects, particularly in stalagmite WC with bi-monthly  
493 resolution. Seasonally driven ventilation effects are likely to lead to higher  $\delta^{18}\text{O}_{\text{spel}}$  and  
494  $\delta^{13}\text{C}_{\text{spel}}$  due to changing the relative  $\text{pCO}_2$  and determining the rate of degassing  $\text{CO}_2$  from a  
495 thin film of water (Baker et al., 2011; Deininger et al., 2012; Scholz et al., 2012). Annual  
496 trends in isotopic composition have been observed in speleothems in well-ventilated caves  
497 (Mattey et al 2008). However, there is no annual periodicity in  $\delta^{18}\text{O}_{\text{spel}}$  or  $\delta^{13}\text{C}_{\text{spel}}$  in  
498 stalagmites WC and WB and ventilation is therefore an unlikely cause for the higher  $\delta^{18}\text{O}_{\text{spel}}$   
499 observed here. Instead, it is likely that the interplay of supersaturation and drip rate are the  
500 dominant controls on growth rate and disequilibrium fractionation.

501

### 502 **5.2.2 Kinetic isotope fractionation effects during precipitation**

503 Cave parameters other than relative humidity and wind velocity may also cause  $\delta^{18}\text{O}_{\text{spel}}$  to  
504 deviate from isotope equilibrium precipitation e.g. temperature, drip interval, drip water  
505 supersaturation with respect to calcite (Day and Hendersen (2011), Dreybrodt and Scholz  
506 (2011) and Deininger et al. (2012)). The estimated theoretical equilibrium of precipitation at  
507 Cathedral Cave using the measured precipitation-weighted mean annual rainfall is -4.89 ‰  
508 VPDB ( $\delta^{18}\text{O}_{\text{precip}}$ ). This is calculated using the equation of Kim and O'Neil (1997), which  
509 does not account for in-cave processes in its formulation. The majority of  $\delta^{18}\text{O}_{\text{spel}}$  values for

510 stalagmite WB and all  $\delta^{18}\text{O}_{\text{spel}}$  values for stalagmite WC are greater than the predicted  
511 equilibrium value, with relative overall offsets of 0.8 ‰ and 1.3 ‰, respectively. This  
512 suggests that stalagmite  $\delta^{18}\text{O}_{\text{spel}}$  rarely if ever reflects the mean isotopic composition of  
513 precipitation at Cathedral Cave. Furthermore, the overall relationship between  $\delta^{18}\text{O}_{\text{spel}}$  and  
514  $\delta^{13}\text{C}_{\text{spel}}$ , an indicator for disequilibrium processes (Dreybrodt and Scholz, 2011), over the  
515 whole time series for stalagmite WC is strong ( $r^2 = 0.77$ ) and likely precipitates under greater  
516 disequilibrium conditions (Figure 5). WB shows no relationship ( $r^2 = 0.00$ ) and likely  
517 precipitates closer to equilibrium conditions (Figure 5).

518

519 High drip water  $\text{pCO}_2$  can cause  $\delta^{18}\text{O}_{\text{spel}}$  to deviate from isotope equilibrium due to kinetic  
520 isotope fractionation during calcite precipitation. Evidence for this at Cathedral Cave  
521 includes the fast growth rates for WB and WC (~ 0.53 and ~0.76 mm / a, respectively).  
522 Calcium concentration is one of the driving forces behind growth rate (Baker et al., 1998;  
523 Dreybrodt, 1999; Baker et al., 2016b) and high mean drip Ca concentration ~2.2 mmol / L<sup>-1</sup>  
524 (Baker et al., 2016b) is also observed. Changes in drip water  $\text{pCO}_2$  can occur over time,  
525 which in turn could control the amount of kinetic isotope fractionation and changes in  $\delta^{18}\text{O}_{\text{spel}}$   
526 over time. Prior calcite precipitation (PCP), vegetation cover, fire, and vadose zone microbial  
527 and root respiration (Baker et al., 2016b) can all control the degree of host rock dissolution  
528 and potentially the extent of drip water  $\text{pCO}_2$ . At Wellington, fire has not been experienced at  
529 the site and thus can be ruled out as an important process. Trees present over the cave are  
530 potentially providing an additional source of vadose zone  $\text{CO}_2$  at Cathedral Cave, and their  
531 regrowth over several decades could lead to long-term changes in drip water  $\text{pCO}_2$  and  
532  $\delta^{18}\text{O}_{\text{spel}}$  over time through changes in the amount of root respiration. Field observations  
533 reveal the stagnant chamber adjacent to South Passage has consistently high  $\text{CO}_2$  (up to  
534 ~50,000 ppm), and deep tap roots from large eucalyptus trees growing on the surface (e.g.

535 above WC; Figure 3; Panel K) are clearly visible in neighbouring Gaden Cave. Over shorter  
536 time periods, variations in PCP could be an important control drip water pCO<sub>2</sub> and associated  
537 kinetic isotope fractionation during calcite precipitation. With intermittent recharge at the  
538 site, there is adequate time for PCP to occur in the karst stores supplying drip water to WB  
539 and WC, and in drier conditions, Ca remaining in solution in the drip water is hypothesised to  
540 decrease due to PCP. The extent of PCP at the site is currently poorly constrained.

541

542 Drip interval is also important in kinetic fractionation as it determines the replenishment rate  
543 of solution on top of the stalagmite, and the isotope fractionation potential is a time  
544 dependent process controlled by the solution residence time (Mühlinghaus et al., 2007, 2009;  
545 Hartmann and Baker, 2017). Longer drip intervals may have a significant effect on enriching  
546 <sup>18</sup>O and <sup>13</sup>C due to Rayleigh distillation processes (Mickler et al., 2006; Mühlinghaus et al.,  
547 2009). Specifically, it is the increasing enrichment in the HCO<sub>3</sub><sup>-</sup> reservoir resulting from  
548 degassing and subsequent CaCO<sub>3</sub> precipitation (Mickler et al., 2006). Mickler et al. (2006)  
549 observed progressive increases in δ<sup>18</sup>O away from the growth axis, as high as +1.7 ‰. Day  
550 and Henderson (2011) estimated ~+1.5 ‰ enrichments in <sup>18</sup>O induced from the combination  
551 of both rapid DIC depletion and evaporation. For very slow drip rates (~1 drip / 50 min)  
552 isotopic exchange with the cave atmosphere is also important and will cause the upper layers  
553 of solution to be in equilibrium with cave atmosphere (Scholz et al., 2009; Dreybrodt et al.,  
554 2011). However, this is less likely to be important here as the average drip rate in South  
555 Passage is between 0 and 0.2 drips / min (Cuthbert et al., 2014a) and is usually > 1 drip / 15  
556 min.

557

558 A conceptual model for dryland caves using Cathedral Cave and stalagmites WC and WB as  
559 an example is shown in Figure 7. The effects of both in-cave disequilibrium processes and

560 epikarst evaporation shift  $\delta^{18}\text{O}_{\text{spel}}$  in the same direction; towards higher values with respect to  
561 precipitation-weighted mean annual rainfall. Both processes will be enhanced during drier  
562 phases. Disequilibrium fractionation can provide one explanation for the positive offset of  
563 WC  $\delta^{18}\text{O}_{\text{spel}}$  relative to WB, as well as the contrasting  $\delta^{18}\text{O}$  vs.  $\delta^{13}\text{C}$  relationship, as WC is  
564 hydrologically fed by a different store which is likely a smaller overflow, evidenced by its  
565 slower drip rate and the fact that it stops dripping in drier periods. This may be due to its  
566 position directly beneath a large eucalyptus tree (Figure 3, Panel K) where roots have  
567 penetrated to access the water store. Although not visible in this cave, there are roots clearly  
568 visible at a similar depth in neighbouring Gaden Cave and similar observations have been  
569 made in Golgotha Cave, SW Western Australia (Treble et al., 2016). Disequilibrium alone  
570 cannot account for the magnitude of variability  $>2\text{‰}$  in  $\delta^{18}\text{O}_{\text{spel}}$ , suggesting that the  
571 influence of epikarst evaporation observed in drip waters (Cuthbert et al., 2014a; Markowska  
572 et al., 2016) is also important for the stalagmite  $\delta^{18}\text{O}_{\text{spel}}$  variability.

573

### 574 *5.2.3 Climate signals in $\delta^{18}\text{O}$*

575 Two significant hydrological drought periods occurred over the stalagmite growth period; the  
576 “Millennium Drought” (1997-2010 CE) and the “WWII Drought” (1937-1945 CE). The  
577 Millennium Drought was characterized by increases in PE, warmer temperatures, water  
578 deficits (decreasing P-ET), an unusually long succession of positive IOD phases (Figure 6;  
579 Ummenhofer et al., (2011)) and a decrease in the rainfall intensity, rather than the number of  
580 rain days (Verdon-Kidd and Kiem, 2009). However, it is suggested that the WWII Drought  
581 (1937-1945 CE) was more severe in intensity than the Millennium Drought (Jonathan et al.,  
582 2015). It was also a precursor to the largest rainfall deficit period (1947-49 CE) during the  
583 WB stalagmite growth period and was characterised by a persistent 10-year decline in CRD  
584 (Figure 6). Whilst both droughts exhibit negative P-ET, suggesting rainfall deficits, the



585 Millennium Drought, in terms of P-ET, appears to be drier. In contrast, the WWII Drought  
586 was characterised by a persistent 10-year decline in CRD (Figure 6) and the greatest negative  
587 cumulative departures from mean rainfall, suggesting depleted groundwater reservoirs. This  
588 is in direct contrast to the Millennium Drought, which had a slightly positive CRD,  
589 suggesting groundwater reservoirs were less negatively impacted, despite drought conditions.

590

591 The fabric of stalagmite WB during the decline in CRD over 1937 to 1947 CE contains  
592 microsparite layers (Figure 3; Panels E, I, J). Microsparite forms via episodes of nucleation  
593 via nanocrystal aggregates, often involving biomediation, which occurs during slow to no  
594 drip periods or during prolonged dry phases (Frisia, 2015). This supports the evidence that  
595 the karst aquifer feeding WB was likely declining in response to this drought period.

596 However,  $\delta^{18}\text{O}_{\text{spel}}$  over the drought period was not significantly higher compared to the  
597 arithmetic mean (WB, Figure 6). Positive trends accelerated several years later, for example  
598 in 1948 CE when  $\delta^{18}\text{O}_{\text{spel}}$  reached -3.3 ‰, coinciding with the highest negative rainfall  
599 departures (low CRD, Figure 6). Similarly, after significant rainfall during the 1950's, which  
600 led to increased deep drainage,  $\delta^{18}\text{O}_{\text{spel}}$  fluctuated by 1-2 ‰, but continued an upward trend  
601 to a maximum of -2.5 ‰ in 1954 CE (WB, Figure 6), before the recharge response occurs.

602 These responses suggest that there is a lag between surface rainfall and karst store recharge,  
603 where low karst store volumes persist even after surface drought conditions had abated, thus  
604 allowing them to be more susceptible to epikarst evaporation and subsequent  $^{18}\text{O}_{\text{water}}$   
605 enrichment. This may imply that a large reservoir is feeding stalagmite WB, which became  
606 depleted in volume over the drought period, and took a long time to be refilled. As a result,  
607 when the karst reservoir was in this low volume phase, the stored water may be more  
608 sensitive to karst evaporative enrichment due to larger air-filled voids and conditions suitable  
609 for PCP, shown in Figure 7. Consequently, stalagmite  $\delta^{18}\text{O}_{\text{spel}}$  correlations to dry surface

610 climate conditions are drawn out due to an apparent persistence or memory effect of previous  
611 conditions or due to non-linear responses to changes in climate. The stalagmite record  
612 suggests that it took a decade after the drought abated (1945 CE) for karst store volumes to  
613 significantly increase, because although there is evidence of recharge from high rainfalls in  
614 the 1950's (Figure 6), the  $\delta^{18}\text{O}_{\text{spel}}$  trend continues to rise, and fabric contains microsparite  
615 layers until the 1955 CE flood. The effect of this drought on long-term store levels might  
616 have been more impactful than the Millennium Drought, although there is no data from years  
617 after the Millennium Drought as the stalagmite was removed from the cave in 2010 CE.  
618 However, stalagmite fabric precipitated during the Millennium Drought contained no  
619 microsparite layers, perhaps suggesting that its impact on the shallow karst water reservoir  
620 was not as extreme.

621

#### 622 *5.2.4 Karst $\delta^{18}\text{O}$ modelling*

623 A combined SMB-karst model was employed to determine whether  $\delta^{18}\text{O}_{\text{spel}}$  can be modelled,  
624 using epikarst evaporation of water as the major driver dominating trends in  $\delta^{18}\text{O}_{\text{spel}}$  by  
625 raising  $\delta^{18}\text{O}_{\text{drip}}$ . The parameterisation of the karst model has been optimised in Cuthbert et al.,  
626 (2014a) for this field site. The model results are shown in Figure 8 and a model schematic is  
627 shown in Supplemental Material in Figure S2. Comparing first the model output for  
628 stalagmite WC,  $\delta^{18}\text{O}_{\text{modelled}}$  is generally in good agreement with  $\delta^{18}\text{O}_{\text{spel}}$ . Almost all major  
629 peaks and troughs could be replicated within the age uncertainty ( $\pm 2.65$  years) suggesting  
630 that epikarst evaporation provides a good explanation for the variability in WC  $\delta^{18}\text{O}_{\text{spel}}$ . One  
631 peak in  $\delta^{18}\text{O}_{\text{spel}}$  in 2001 CE was not captured in  $\delta^{18}\text{O}_{\text{modelled}}$  but all five subsequent peaks were  
632 within  $\pm 1$  years of  $\delta^{18}\text{O}_{\text{spel}}$ . There is an offset of  $\sim 0.5 - 1$  ‰ between WC  $\delta^{18}\text{O}_{\text{modelled}}$  and  
633  $\delta^{18}\text{O}_{\text{spel}}$  values (e.g. 1990 CE). This may be because the model only considered karst  
634 evaporation and temperature dependent fractionation (Kim and O'Neil, 1997) as the two main

635 drivers of  $\delta^{18}\text{O}_{\text{spel}}$  variability, and not potential additional kinetic effects. The co-variation of  
636 WC  $\delta^{18}\text{O}_{\text{modelled}}$  and  $\delta^{18}\text{O}_{\text{spel}}$  values here strongly suggest that WC can be explained by a  
637 simple single-reservoir model, which is very sensitive to karst evaporation and changes in  
638 water storage volumes, controlled by alternating periods of recharge and decline.

639

640 Conversely, WB  $\delta^{18}\text{O}_{\text{modelled}}$  and  $\delta^{18}\text{O}_{\text{spel}}$  values are less in agreement (Figure 8). The first  
641 peak in  $\delta^{18}\text{O}_{\text{modelled}}$  does not appear in  $\delta^{18}\text{O}_{\text{spel}}$ , although it coincides with the stalagmite  
642 growth nucleation phase. Otherwise, the first part of the WB  $\delta^{18}\text{O}_{\text{modelled}}$  time series is  
643 generally in good agreement with  $\delta^{18}\text{O}_{\text{spel}}$  until ~1950 CE. As expected, given the prescribed  
644 depleted isotopic input for large rainfall events, the 1955 CE flood is captured with similar  
645 magnitude to the observed  $\delta^{18}\text{O}_{\text{spel}}$ . The long stable period from 1970-1990 CE also shows  
646 good agreement with WB  $\delta^{18}\text{O}_{\text{modelled}}$  and  $\delta^{18}\text{O}_{\text{spel}}$ , although  $\delta^{18}\text{O}_{\text{modelled}}$  is offset in some parts  
647 by up to 0.5 ‰. The Millennium Drought, which is captured as a rising trend punctuated by  
648 troughs and peaks in  $\delta^{18}\text{O}_{\text{modelled}}$  for WC, is not well represented by the model for WB.

649 Complex flow behaviour, variable lags and have been demonstrated in this cave system  
650 (Markowska et al., 2016). This suggests that WB cannot be explained by a simple single-  
651 reservoir model and likely is fed by multiple reservoirs. WB's position in the cave, behind a  
652 large flowstone feature, which has grown over the entire Quaternary period, suggests a  
653 possible connection to a larger storage reservoir. Thus, while the model used can provide  
654 insights into the likely processes controlling  $\delta^{18}\text{O}_{\text{spel}}$ , it also likely points to the necessity of  
655 (1) a more complex multi-store model to capture the variability in WB, (2) quantification of  
656 disequilibrium processes from additional cave monitoring of drips feeding WB and WC, and  
657 (3) a longer time series of drip water isotope data for model calibration before the model can  
658 reliably hindcast past droughts and recharge events.

659

660 The selection of speleothems for analysis is subject to trade-offs due to the sensitivity of  
661  $\delta^{18}\text{O}_{\text{spel}}$  to epikarst evaporation and volume and discontinuous growth, where smaller near-  
662 surface reservoirs with large headspaces will show the greatest epikarst evaporation  
663 sensitivity but also may be more likely to exhibit discontinuous growth by virtue of their  
664 small storage volumes. Figure 9 shows the relationship between the modelled offset in  $\delta^{18}\text{O}$   
665 from the mean rainfall composition due to epikarst evaporation, the water storage depth  
666 where epikarst evaporation ‘switches on’ (S2lim) and the epikarst evaporation rate (mm/d).  
667 The location of the two stalagmites from this study are shown in this parameter space (Figure  
668 9). For a water-limited environment as modelled here, the amount of epikarst evaporation is a  
669 small fraction of the total karst water balance, and the continuity of speleothem growth can  
670 be assumed to be solely a function of the storage volume via S2lim. Assuming that our 1D  
671 model store approximates to the actual 3-dimensional karst void, then the more sensitive a  
672 stalagmite is to evaporation the more likely it is to have discontinuous growth or longer  
673 hiatuses. At Wellington Caves, the near vertical bedding combined with hypogene solution  
674 features means that the development of vertical voids is a reasonable conceptualisation.  
675 Figure 9 shows that WC  $\delta^{18}\text{O}$  will be more affected by karst evaporation processes compared  
676 to WB. Therefore, WC is more sensitive to climatic influences including changes in water  
677 balance. Similarly, climatically sensitive samples, potentially identified through fabric  
678 analysis, could therefore be more useful for paleoclimate applications.

679

## 680 **6. Conclusion**

681 This study reveals that the use of  $\delta^{18}\text{O}_{\text{spel}}$  as a source of paleoenvironmental information does  
682 not require the prerequisite that speleothems formed under isotopic equilibrium conditions.  
683 However, coeval stalagmites oxygen isotope records have differences that we relate to their  
684 individual hydrology and flow path, demonstrating that in a water-limited environment,

685  $\delta^{18}\text{O}_{\text{spel}}$  can be sensitive to hydrological changes at the individual drip level. Because of this,  
686 replication of coeval stalagmites oxygen isotope records may be lower in dryland caves  
687 compared to caves with well-mixed large water storage reservoirs from temperate  
688 environments. This is conceptually demonstrated in Figure 7, by showing the relative sizes of  
689 water stores feeding drips WC and WB during dry conditions. In Figure 7 the overflow store  
690 feeding WC, is quickly depleted in dry conditions as opposed to WB, which is connected to a  
691 more consistent water source and fed via multiple flow routes.

692

693 In semi-arid environments sensitive to water balance changes, epikarst evaporation and  
694 disequilibrium fractionation from kinetic effects are likely to lead to  $^{18}\text{O}$  enrichment during  
695 drier phases. Epikarst evaporation driven fractionation is controlled by changes to water  
696 balance and rainfall amount on the surface which has lag times before being expressed in the  
697 stalagmite record. This is more important in dry or drought conditions (e.g. Millennium  
698 Drought; Figure 6) where storage volumes are low and larger air pockets develop as stores  
699 decline (Figure 7). However, the timing of the  $\delta^{18}\text{O}_{\text{spel}}$  response to dry surface conditions  
700 suggests that they are out-of-phase with the actual occurrence of drought periods on the  
701 surface (Figure 6; e.g. WB, peak  $\delta^{18}\text{O}_{\text{spel}}$  occurs ~9 years after the end of the WWII Drought).  
702 Thus, the interpretation of  $\delta^{18}\text{O}_{\text{spel}}$  represents water balance excursions but lagged due to  
703 inertia of the vadose zone in its response to surface climate changes.

704

705 Stalagmites in this study show that  $\delta^{18}\text{O}_{\text{spel}}$  is sensitive to changes in hydroclimate or water  
706 balance, resulting in isotopic enrichment as a direct result of drying conditions – thus  
707 preserving the isotopic impact of reduced recharge. This differs from a classic direct  
708 interpretation of the  $\delta^{18}\text{O}_{\text{spel}}$  as a proxy for rainfall amount. Large modifications of the  
709 original  $\delta^{18}\text{O}_{\text{precip}}$  value occurs in this water-limited cave system, from both the karst and the

710 cave environment, and consequently cave monitoring is essential to ascertain the dominant  
711 processes that affect  $\delta^{18}\text{O}_{\text{spel}}$ . The combination of epikarst evaporation and kinetic isotope  
712 effects in the cave e.g. resulting from a rapid loss of  $\text{CO}_2$  or change in drip interval, are likely  
713 to positively shift  $\delta^{18}\text{O}_{\text{spel}}$  in the same direction and thus these disequilibrium stalagmites in  
714 dryland environments may be useful as past water balance or paleorecharge records.

715

716 The significant flood event affecting most of SE Australia in 1955 CE was recorded in  
717 stalagmite WB, suggesting that these stalagmites, because of their sensitivity to water balance  
718 changes, may be very suitable archives of extreme pluvials or floods. Rainfall in this region is  
719 strongly governed by ENSO, where La Niña's have a more significant influence on the  
720 intensity and duration of rainfall events than El Niño's. Thus, paleorecharge records from  
721 Wellington Caves would be useful for providing evidence of the frequency and severity of  
722 past pluvial and drought periods. Such records may be important in determining  
723 paleoprecipitation anomalies and could be used to elucidate the relationship of climatic  
724 dynamics with rainfall over SE Australia.

725

## 726 **Acknowledgements**

727 Thank you to the Dubbo Regional Council and continued support of cave staff and  
728 management at Wellington Caves. Thank you to Dr. Peter Graham for collecting  
729 instantaneous rainfall samples and to Dr. Catherine Jex for analysing the rainfall samples.  
730 AB, MM and MSA were partly supported by the ARC/NWC National Centre for  
731 Groundwater Research and Training. SF acknowledges the support of DP 160101058. The  
732 outcomes of this study contribute to ARC Discovery Project DP140102059 awarded to PCT.  
733 MOC was supported by the European Community's Seventh Framework Programme

734 [FP7/2007–2013] under grant agreement No.299091 and by an Independent Research  
735 Fellowship from the UK Natural Environment Research Council (NE/P017819/1).

736

737 **References**

738

739 Anderson, W. T., Bernasconi, S.M., McKenzie, J.A., and Saurer, M. (1998). Oxygen and  
740 carbon isotopic record of climatic variability in tree ring cellulose (*Picea abies*): An  
741 example from central Switzerland (1913–1995). *J. Geophys. Res-Atmos* **103(D24)**,  
742 31625-31636.

743 Australian Bureau of Statistics (2008) *1301.0 - Yearbook Complete, 2008 Natural Disasters*  
744 *in Australia, Article 4*. Retrieved from:

745 [http://www.abs.gov.au/AUSSTATS/abs@.nsf/7d12b0f6763c78caca257061001cc588/fe  
cb2ab6de16171eca2570de0005871b!OpenDocument](http://www.abs.gov.au/AUSSTATS/abs@.nsf/7d12b0f6763c78caca257061001cc588/fe<br/>746 cb2ab6de16171eca2570de0005871b!OpenDocument)

747 Ayalon, A., Bar-Matthews, M. and Sass, E. (1998). Rainfall-recharge relationships within a  
748 karstic terrain in the Eastern Mediterranean semi-arid region, Israel:  $\delta^{18}\text{O}$  and  $\delta\text{D}$   
749 characteristics. *J. Hydrol.* **207**, 18-31.

750 Baker, A., Genty, D., Dreybrodt, W., Barnes, W.L., Mockler, N.J. and Grapes, J., 1998.

751 Testing Theoretically Predicted Stalagmite Growth Rate with Recent Annually  
752 Laminated Samples: Implications for Past Stalagmite Deposition. *Geochim. Cosmochim.*  
753 *Acta* **62**, 393-404.

754 Baker, A., Wilson, R., Fairchild, I.J., Franke, J., Spötl, C., Matthey, D., Trouet, V., and

755 Fuller, L. (2011). High resolution  $\delta^{18}\text{O}$  and  $\delta^{13}\text{C}$  records from an annually laminated

756 Scottish stalagmite and relationship with last millennium climate. *Global Planet. Change*  
757 **79**, 303-311.

758 Baker, A., Jex, C.N., Rutledge, H., Woltering, M., Blyth, A.J., Andersen, M.S., Cuthbert,  
759 M.O., Marjo, C.E., Markowska, M., Rau, G.C. and Khan, S.J. (2016a). An irrigation  
760 experiment to compare soil, water and speleothem tetraether membrane lipid  
761 distributions. *Org. Geochem.* **94**, 12-20.

762 Baker, A., Flemons, I., Andersen, M.S., Coleborn, K. and Treble, P.C. (2016b). What  
763 determines the calcium concentration of speleothem-forming drip waters? *Global Planet.*  
764 *Change* **143**, 152-161.

765 Baker, A., Hartmann, A., Duan, W., Hankin, S., Comas-Bru, L., Cuthbert, M.O., Treble,  
766 P.C., Banner, J., Genty, D., Baldini, L., Bartolomé, M., Moreno, A., and Pérez-Mejías,  
767 C. Global distribution and controls on cave drip water oxygen isotope composition.  
768 *Nature Communications*, **10**, Article number: 2984

769 Baker, A.J., Matthey, D.P. and Baldini, J.U.L. (2014). Reconstructing modern stalagmite  
770 growth from cave monitoring, local meteorology, and experimental measurements of  
771 dripwater films. *Earth Planet. Sci. Lett.* **392**, 239-249.

772 Bar-Matthews, M., Ayalon, A., Matthews, A., Sass, E. and Halicz, L. (1996). Carbon and  
773 oxygen isotope study of the active water-carbonate system in a karstic Mediterranean  
774 cave: Implications for paleoclimate research in semiarid regions. *Geochim. Cosmochim.*  
775 *Acta* **60**, 337-347.

776 Bar-Matthews, M., Ayalon, A., Gilmour, M., Matthews, A. and Hawkesworth, C.J. (2003).  
777 Sea-land oxygen isotopic relationships from planktonic foraminifera and speleothems in  
778 the Eastern Mediterranean region and their implication for paleorainfall during  
779 interglacial intervals. *Geochim. Cosmochim. Acta* **67**, 3181-3199.

780 Benavente, J., Vadillo, I., Carrasco, F., Soler, A., Liñán, C. and Moral, F. (2010). Air  
781 Carbon Dioxide Contents in the Vadose Zone of a Mediterranean Karst. *Vadose Zone J.*  
782 **9**, 126-136.



783 Berthelin, R., Rinderer, M., Andreo, B., Baker, A., Kilian, D., Leonhardt, G., Lotz, A.,  
784 Lichtenwoehr, K., Mudarra, M., Padilla, I. Y., Pantoja Agreda, F., Rosolem, R., Vale,  
785 A., and Hartmann, A.: A soil moisture monitoring network to characterize karstic  
786 recharge and evapotranspiration at five representative sites across the globe, *Geosci.*  
787 *Instrum. Method. Data Syst. Discuss.*, <https://doi.org/10.5194/gi-2019-22>

788 Bureau of Meteorology (2010). *Rainfall Deciles (AWA grids 1900-pres) February 1955*.  
789 Retrieved from: <http://www.bom.gov.au/climate/enso/lnlist/195457/195502.gif> .

790 Bureau of Meteorology (2011). *Australian Water resources Assessment 2010*. Retrieved  
791 from: <http://www.bom.gov.au/water/awra/2010/documents/assessment-low.pdf>

792 Bureau of Meteorology (2015). *Recent rainfall, drought and southern Australia's long-term*  
793 *rainfall decline*. Retrieved from: [http://www.bom.gov.au/climate/updates/articles/a010-](http://www.bom.gov.au/climate/updates/articles/a010-southern-rainfall-decline.shtml)  
794 [southern-rainfall-decline.shtml](http://www.bom.gov.au/climate/updates/articles/a010-southern-rainfall-decline.shtml) Bureau of Meteorology (2019). *Southern Oscillation*  
795 *Index (SOI) since 1876*. Retrieved from:  
796 <http://www.bom.gov.au/climate/current/soihtml.shtml>

797 Bureau of Meteorology (2019a). *Indian Ocean influences on Australian climate*. Retrieved  
798 from: <http://www.bom.gov.au/climate/iod/>

799 Butterworth, J. A., Schulze, R. E., Simmonds, L. P., Moriarty, P., and Mugabe, F.:  
800 Hydrological processes and water resources management in a dryland environment IV:  
801 Long-term groundwater level fluctuations due to variation in rainfall, *Hydrol. Earth Syst.*  
802 *Sci.*, 3, 353–361, <https://doi.org/10.5194/hess-3-353-1999>, 1999.

803 Cai, Y., Cowan, T., Briggs, P.R. and Raupach, M.R. (2009). Rising temperature depletes soil  
804 moisture and exacerbates severe drought conditions across southeast Australia. *Geophys.*  
805 *Res. Lett.* **36** L21709.

806 Christensen, J.H., K. Krishna Kumar, Marshall, G., Turner, J. (2013). Climate Phenomena  
807 and their Relevance for Future Regional Climate Change. In: Stocker, T.F., D. Qin, G.-K.  
808 Plattner, M. Tignor, S.K. Allen, J. Boschung, A. Nauels, Y. Xia, V. Bex and P.M.  
809 Midgley (eds.) *The Physical Science Basis. Contribution of Working Group I to the Fifth*  
810 *Assessment Report of the Intergovernmental Panel on Climate Change 2013*. Cambridge,  
811 UK and New York, NY: Cambridge University Press, 1217-1308.

812 Clarke, H., Lucas, C. and Smith, P. (2013). Changes in Australian fire weather between 1973  
813 and 2010. *Int. J. Climatol.* **33**, 931-944.

814 Coplen, T.B. (1988). Normalization of oxygen and hydrogen isotope data. *Chem. Geol.:*  
815 *Isotope Geoscience* **72**, 293-297.

816 Coplen, T.B. (2007). Calibration of the calcite–water oxygen-isotope geothermometer at  
817 Devils Hole, Nevada, a natural laboratory. *Geochim. Cosmochim. Acta* **71**, 3948-3957.

818 Crosbie, R.S., Pickett, T., Mpelasoka, F.S., Hodgson, G., Charles, S.P. and Barron, O.V.  
819 (2013). An assessment of the climate change impacts on groundwater recharge at a  
820 continental scale using a probabilistic approach with an ensemble of GCMs. *Climatic*  
821 *Change* **117**, 41-53.

822 Cuthbert, M., Mackay, R. and Nimmo, J. (2013). Linking soil moisture balance and source-  
823 responsive models to estimate diffuse and preferential components of groundwater  
824 recharge. *Hydrol. Earth Syst. Sci.* **17**, 1003-1019.

825 Cuthbert, M.O., Baker, A., Jex, C.N., Graham, P.W., Treble, P.C., Andersen, M.S. and Ian  
826 Acworth, R. (2014a). Drip water isotopes in semi-arid karst: Implications for speleothem  
827 paleoclimatology. *Earth Planet. Sci. Lett.* **395**, 194-204.

828 Cuthbert, M.O., Rau, G.C., Andersen, M.S., Roshan, H., Rutledge, H., Marjo, C.E.,  
829 Markowska, M., Jex, C.N., Graham, P.W., Mariethoz, G., Acworth, R.I. and Baker, A.  
830 (2014b). Evaporative cooling of speleothem drip water. *Sci. Rep.* **4**, 5162.

831 D'Odorico, P. and Porporato, A. (2006). *Dryland Ecohydrology*. New York, NY: Springer-  
832 verlag.

833 Dai, A. (2013). Increasing drought under global warming in observations and models. *Nature*  
834 *Clim. Change* **3**, 52-58.

835 Dansgaard, W. (1964). Stable isotopes in precipitation. *Tellus* **16**, 436-468.

836 Day, C.C. and Henderson, G.M. (2011). Oxygen isotopes in calcite grown under cave-  
837 analogue conditions. *Geochim. Cosmochim. Acta* **75**, 3956-3972.

838 Deininger, M., Fohlmeister, J., Scholz, D. and Mangini, A. (2012). Isotope disequilibrium  
839 effects: The influence of evaporation and ventilation effects on the carbon and oxygen  
840 isotope composition of speleothems – A model approach. *Geochim. Cosmochim. Acta* **96**,  
841 57-79.

842 Deininger, M. and Scholz, S. (2019). ISOLUTION 1.0: an ISOtope evoLUTION model  
843 describing the stable oxygen ( $\delta^{18}\text{O}$ ) and carbon ( $\delta^{13}\text{C}$ ) isotope values of speleothems.  
844 *International Journal of Speleology*, **48**, 21-32.

845 Denniston, R.F., González, L.A., Asmerom, Y., Baker, R.G., Reagan, M.K. and Bettis, E.A.  
846 (1999). Evidence for increased cool season moisture during the middle Holocene.  
847 *Geology* **27**, 815-818.

848 Desmarchelier, J.M., Goede, A., Ayliffe, L.K., McCulloch, M.T. and Moriarty, K. (2000).  
849 Stable isotope record and its palaeoenvironmental interpretation for a late Middle  
850 Pleistocene speleothem from Victoria Fossil Cave, Naracoorte, South Australia. *Quatern.*  
851 *Sci. Rev.* **19**, 763-774.

852 Dietzel, M., Tang, J., Leis, A. and Köhler, S.J. (2009). Oxygen isotopic fractionation during  
853 inorganic calcite precipitation — Effects of temperature, precipitation rate and pH. *Chem.*  
854 *Geol.* **268**, 107-115.

855 Dreybrodt, W. (1999). Chemical kinetics, speleothem growth and climate. *Boreas* **28**, 347-  
856 356.

857 Dreybrodt, W. and Scholz, D. (2011). Climatic dependence of stable carbon and oxygen  
858 isotope signals recorded in speleothems: from soil water to speleothem calcite. *Geochim.*  
859 *Cosmochim. Acta* **75**, 734-752.

860 Even, H., Carmi, I., Magaritz, M. and Gerson, R. (1986). Timing the transport of water  
861 through the upper vadose zone in a Karstic system above a cave in Israel. *Earth Surf.*  
862 *Proc. Land.* **11**, 181-191.

863 Fawcett, R.J.B., Trewin, B.C., Braganza, K., Smalley, R.J., Jovanovic, B. and Jones, D.A.  
864 (2012). *On the sensitivity of Australian temperature trends and variability to analysis*  
865 *methods and observation networks, CAWCR Technical Report* (Report no. 050).  
866 Aspendale, VIC: The Centre for Australian Weather and Climate Research.

867 Feng, S. and Fu, Q. (2013). Expansion of global drylands under a warming climate. *Atmos.*  
868 *Chem. Phys.* **13**, 10081-10094.

869 Fleitmann, D., Burns, S.J., Neff, U., Mudelsee, M., Mangini, A. and Matter, A. (2004).  
870 Palaeoclimatic interpretation of high-resolution oxygen isotope profiles derived from  
871 annually laminated speleothems from Southern Oman. *Quatern. Sci. Rev.* **23**, 935-945.

872 Friedman, I. and O'Neil, J.R. (1977). *Compilation of stable isotope fractionation factors of*  
873 *geochemical interest* (Report no. 440-KK). Washington, DC: U.S. Geological Survey.

874 Frisia, S. (2015). Microstratigraphic logging of calcite fabrics in speleothems as tool for  
875 palaeoclimate studies. *Intern. J. Speleology* **44**, 1-16.

876 Frisia, S., Borsato, A and Hellstrom, J. (2018) High spatial resolution investigation of  
877 nucleation, growth and early diagenesis in speleothems as exemplar for sedimentary  
878 carbonates. *Earth Sci. Rev.* **178**, 68-91.

879 Gonfiantini, R. (1984). *Advisory Group Meeting on Stable Isotope Reference Samples for*  
880 *Geochemical and Hydrological Investigations* (Report to the Director General of the  
881 International Atomic Energy Agency). Vienna, WIE: IAEA.

882 Gonfiantini, R. (1986). Chapter 3 – Environmental isotopes in lake studies In: Fontes, J.C.  
883 (Ed.), *The Terrestrial Environment*, (pp. 113-168). Amsterdam, NH: Elsevier.

884 Hartmann, A. and Baker, A. (2017). Modelling karst vadose zone hydrology and its relevance  
885 for paleoclimate reconstruction. *Earth Sci. Rev.* **172**, 178-192.

886 Huang, J., Ji, M., Xie, Y., Wang, S., He, Y. and Ran, J., 2016. Global semi-arid climate  
887 change over last 60 years. *Clim. Dynam.* **46**, 1131-1150.

888 Hut, G. (1987). *Consultants' Group Meeting on Stable Isotope Reference Samples for*  
889 *Geochemical and Hydrological Investigations*, Report to the Director General of the  
890 International Atomic Energy Agency. Vienna, WIE: IAEA.

891 Jex, C.N., Mariethoz, G., Baker, A., Graham, P.W., Andersen, M.S., Acworth, R.I., Edwards,  
892 N. and Azcurra, C. (2012). Spatially dense drip hydrological monitoring and infiltration  
893 behaviour at the Wellington Caves, South East Australia. *Int. J. Speleol.* **41**, 283-296.

894 Jolly, W.M., Cochrane, M.A., Freeborn, P.H., Holden, Z.A., Brown, T.J., Williamson, G.J.  
895 and Bowman, D.M.J.S. (2015). Climate-induced variations in global wildfire danger from  
896 1979 to 2013. *Nature Comms.* **6**, 7537.

897 Kaufman, A., Bar-Matthews, M., Ayalon, A. and Carmi, I. (2003). The vadose flow above  
898 Soreq Cave, Israel: a tritium study of the cave waters. *J. Hydrol.* **273**, 155-163.

899 Keshavarzi, M., 2017. Assessing hydraulic connection and dissolved organic matter in a karst  
900 landscape: Wellington, Australia. Unpublished PhD, UNSW.  
901 <http://handle.unsw.edu.au/1959.4/59756>

902 Kim, S. and O'Neil, J.R. (1997). Equilibrium and nonequilibrium oxygen isotope effects in  
903 synthetic carbonates. *Geochim. Cosmochim. Acta* **61**, 3461-3475.

904 King, A.D., Alexander, L.V. and Donat, M.G. (2013). Asymmetry in the response of eastern  
905 Australia extreme rainfall to low-frequency Pacific variability. *Geophys. Res. Lett.* **40**,  
906 2271-2277.

907 Lange, J., Greenbaum, N., Husary, S., Ghanem, M., Leibundgut, C. and Schick, A.P. (2003).  
908 Runoff generation from successive simulated rainfalls on a rocky, semi-arid,  
909 Mediterranean hillslope. *Hydrol. Procs.* **17**, 279-296.

910 Markowska, M., Baker, A., Andersen, M. S., Jex, C. N., Cuthbert, M. O., Rau, Gabriel C.,  
911 Graham, P. W., Rutledge, H., Mariethoz, G., Marjo, C. E., Treble, Pauline C., and  
912 Edwards, N. (2016). Semi-arid zone caves: Evaporation and hydrological controls on  
913  $\delta^{18}\text{O}$  drip water composition and implications for speleothem paleoclimate  
914 reconstructions. *Quatern. Sci. Rev.* **131**, 285-301.

915 Markowska, M., Fohlmeister, J., Treble, P.C., Baker, A., Andersen, M.S. and Hua, Q. (2019).  
916 Modelling the 14C bomb-pulse in young speleothems using a soil carbon continuum  
917 model, *Geochim. Cosmochim. Acta*, doi.org/10.1016/j.gca.2019.04.029

918 Matthey, D., Lowry, D., Duffet, J., Fisher, R., Hodge, E. and Frisia, S. (2008). A 53 year  
919 seasonally resolved oxygen and carbon isotope record from a modern Gibraltar  
920 speleothem: reconstructed drip water and relationship to local precipitation. *Earth Planet.*  
921 *Sci. Lett.* **269**, 80-95.

922 Matthey, D.P., Fairchild, I.J., Atkinson, T.C., Latin, J.-P., Ainsworth, M. and Durrell, R.  
923 (2010). Seasonal microclimate control of calcite fabrics, stable isotopes and trace  
924 elements in modern speleothem from St Michaels Cave, Gibraltar. *Geol. Soc. Spec. Publ.*  
925 **336**, 323-344.

926 Matthey, D.P., Fisher, R., Atkinson, T.C., Latin, J.P., Durrell, R., Ainsworth, M., Lowry, D.  
927 and Fairchild, I.J. (2013). Methane in underground air in Gibraltar karst. *Earth Planet.*  
928 *Sci. Lett.* **374**, 71-80.

929 McDonough, L.K., Iverach, C.P., Beckmann, S., Manefield, M., Rau, G.C., Baker, A. and  
930 Kelly, B.F.J. (2016). Spatial variability of cave-air carbon dioxide and methane  
931 concentrations and isotopic compositions in a semi-arid karst environment. *Environ.*  
932 *Earth Sci.* **75**, 1-20.

933 Mickler, P.J., Stern, L.A. and Banner, J.L. (2006). Large kinetic isotope effects in modern  
934 speleothems. *Geol. Soc. Am. Bull.* **118**, 65-81.

935 Moquet, J.S., Cruz, F.W., Novello, V.F., Stríkis, N.M., Deininger, M., Karmann, I., Santos,  
936 R.V., Millo, C., Apaestegui, J., Guyot, J.L., Siffedine, A., Vuille, M., Cheng, H.,  
937 Edwards, R.L. and Santini, W. (2016). Calibration of speleothem  $\delta^{18}\text{O}$  records against  
938 hydroclimate instrumental records in Central Brazil. *Global Planet. Change* **139**, 151-  
939 164.

940 Morgan, K., Jankowski, J. and Taylor, G. (2006). Structural controls on groundwater flow  
941 and groundwater salinity in the Spicers Creek catchment, Central West region, New South  
942 Wales. *Hydrol. Procs.* **20**, 2857-2871.

943 Mühlinghaus, C., Scholz, D. and Mangini, A. (2007). Modelling stalagmite growth and  $\delta^{13}\text{C}$   
944 as a function of drip interval and temperature. *Geochim. Cosmochim. Acta* **71**, 2780-2790.

945 Mühlinghaus, C., Scholz, D. and Mangini, A. (2009). Modelling fractionation of stable  
946 isotopes in stalagmites. *Geochim. Cosmochim. Acta* **73**, 7275-7289.

947 Murphy, B.F. and Timbal, B. (2008). A review of recent climate variability and climate  
948 change in southeastern Australia. *Int. J. Clim.* **28**, 859-879.

949 NCC & BoM: National Climate Centre, Bureau of Meteorology (2011). *Frequent heavy rain*  
950 *events in late 2010/early 2011 lead to widespread flooding across eastern Australia.*  
951 Special Climate Statement 24. Retrieved form:  
952 <http://www.bom.gov.au/climate/current/statements/scs24b.pdf>

953 Nicholls, N. (2010). Local and remote causes of the southern Australian autumn-winter  
954 rainfall decline, 1958–2007. *Clim. Dyn.* **34**, 835-845.

955 Pittock, B., Abbs, D., Suppiah, R. and Jones, R. (2006). Climatic Background to Past and  
956 Future Floods in Australia, *Adv. Ecol. Res.* **39**,13-39.

957 Rau, G.C., Cuthbert, M.O., Andersen, M.S., Baker, A., Rutlidge, H., Markowska, M.,  
958 Roshan, H., Marjo, C.E., Graham, P.W. and Acworth, R.I. (2015). Controls on cave drip  
959 water temperature and implications for speleothem-based paleoclimate reconstructions.  
960 *Quatern. Sci. Rev.* **127**, 19-36.

961 Raupach, M.R., Briggs, P.R., Haverd, V., King, E.A., Paget, M. and Trudinger, C.M. (2009).  
962 *Australian Water Availability Project (AWAP): CSIRO Marine and Atmospheric*  
963 *Research Component: Final Report for Phase 3* (CAWCR Technical Report 013),  
964 Canberra, ACT: CSIRO.

965 Raupach, M.R., Briggs, P.R., Haverd, V., King, E.A., Paget, M. and Trudinger, C.M. (2012).  
966 *Australian Water Availability Project*. CSIRO Marine and Atmospheric Research.  
967 Retrieved from: <http://www.csiro.au/awap>

968 Rozanski, K., Araguás-Araguás, L. and Gonfiantini, R. (1993). *Isotopic Patterns in Modern*  
969 *Global Precipitation, Climate Change in Continental Isotopic Records*. Washington, DC:  
970 American Geophysical Union.

971 Rutlidge, H., Baker, A., Marjo, C.E., Andersen, M.S., Graham, P.W., Cuthbert, M.O., Rau,  
972 G.C., Roshan, H., Markowska, M., Mariethoz, G. and Jex, C.N. (2014). Dripwater  
973 organic matter and trace element geochemistry in a semi-arid karst environment:  
974 Implications for speleothem paleoclimatology. *Geochim. Cosmochim. Acta* **135**, 217-230.

975 Rutlidge, H., Andersen, M.S., Baker, A., Chinu, K.J., Cuthbert, M.O., Jex, C.N., Marjo, C.E.,  
976 Markowska, M. and Rau, G.C. (2015). Organic characterisation of cave drip water by LC-  
977 OCD and fluorescence analysis. *Geochim. et Cosmochim. Acta* **166**, 15-28.



978 Scholz, D., Mühlinghaus, C. and Mangini, A., 2009. Modelling  $\delta^{13}\text{C}$  and  $\delta^{18}\text{O}$  in the  
979 solution layer on stalagmite surfaces. *Geochim. Cosmochim. Acta* **73**, 2592- 2602.

980 Scholz, D., Frisia, S., Borsato, A., Spötl, C., Fohlmeister, J., Mudelsee, M., Miorandi, R. and  
981 Mangini, A. (2012). Holocene climate variability in north-eastern Italy: potential  
982 influence of the NAO and solar activity recorded by speleothem data. *Clim. Past* **8**, 1367-  
983 1383.

984 Sheffer, N.A., Cohen, M., Morin, E., Grodek, T., Gimburg, A., Magal, E., Gvirtzman, H.,  
985 Nied, M., Isele, D. and Frumkin, A. (2011). Integrated cave drip monitoring for epikarst  
986 recharge estimation in a dry Mediterranean area, Sif Cave, Israel. *Hydrol. Process.* **25**,  
987 2837-2845.

988 STAP (2010) Report of the Scientific and Technical Advisory Panel to the Fourth GEF  
989 Assembly. Accessed at: [https://www.thegef.org/sites/default/files/council-meeting-  
990 documents/GEF-A.4-3 - Report of STAP 0 1.pdf](https://www.thegef.org/sites/default/files/council-meeting-documents/GEF-A.4-3 - Report of STAP 0 1.pdf)

991 Thorpe, E.W. and Tweedie, A.D. (1956). The N.S.W. floods of February 1955. *Aust. Geogr.*  
992 **6**, 3-13.

993 Trabucco, A. and Zomer, R.J. (2009). Global Aridity Index (Global-aridity) and Global  
994 Potential Evapo-transpiration (Global-PET) Geospatial Database. CGIAR Consortium for  
995 Spatial Information. Available from the CGIAR-CSI GeoPortal at  
996 <http://www.csi.cgiar.org/>.

997 Treble, P.C., Budd, W.F., Hope, P.K. and Rustomji, P.K. (2005). Synoptic-scale climate  
998 patterns associated with rainfall  $\delta^{18}\text{O}$  in southern Australia. *J. Hydrol.* **302**, 270-282.

999 Treble, P.C., Fairchild, I.J., Baker, A., Meredith, K.T., Andersen, M.S., Salmon, S.U.,  
1000 Bradley, C., Wynn, P.M., Hankin, S.I., Wood, A. and McGuire, E. (2016). Roles of forest  
1001 bioproductivity, transpiration and fire in a nine-year record of cave dripwater chemistry  
1002 from southwest Australia. *Geochim. Cosmochim. Acta* **184**, 132-150.

1003 Trewin, B. (2013). A daily homogenized temperature data set for Australia. *Int. J. Clim.* **33**,  
1004 1510-1529.

1005 Ummenhofer, C.C., Sen Gupta, A., Briggs, P.R., England, M.H., McIntosh, P.C., Meyers,  
1006 G.A., Pook, M.J., Raupach, M.R. and Risbey, J.S. (2011). Indian and Pacific Ocean  
1007 Influences on Southeast Australian Drought and Soil Moisture. *J. Clim.* **24**, 1313-1336.

1008 Van Dijk, A.I.J.M., Beck, H.E., Crosbie, R.S., de Jeu, R.A.M., Liu, Y.Y., Podger, G.M.,  
1009 Timbal, B. and Viney, N.R. (2013). The Millennium Drought in southeast Australia  
1010 (2001– 2009): Natural and human causes and implications for water resources,  
1011 ecosystems, economy, and society. *Wat. Res. Res.* **49**, 1040-1057.

1012 Verdon-Kidd, D.C. and Kiem, A.S. (2009). Nature and causes of protracted droughts in  
1013 southeast Australia: Comparison between the Federation, WWII, and Big Dry droughts.  
1014 *Geophys. Res. Lett.* **36**, L22707.

1015 Walker, B. (2010). Dubbo's big flood, gone but not forgotten, *Daily Liberal*. Retrieved from:  
1016 <http://www.dailyliberal.com.au/story/855359/dubbos-big-flood-gone-but-not-forgotten/>

1017 Weber, K., Stewart, M. (2004). A Critical Analysis of the Cumulative Rainfall Departure  
1018 Concept. *Groundwater*. **42** (6); 935-938.

1019 Williamson, G., J., Prior, L., D., Jolly, W.M., Cochrane, M., A., Murphy, B., P., Bowman,  
1020 D.M.J.S. (2016). Measurement of inter- and intra-annual variability of landscape fire  
1021 activity at a continental scale: the Australian case. *Environ. Res. Lett.* **11**, 035003.

1022 **Figure Captions**

1023

1024 Figure 1. Aridity map of Australia compiled with spatial aridity data from Trabucco and  
1025 Zomer (2009). The location of Wellington is shown.

1026

1027 Figure 2. Climate variables over 1930 – 2010 CE. Panels A and B show the monthly  
1028 maximum and minimum temperature anomalies, respectively, derived from the Australian  
1029 Water Availability Project (AWAP) (Raupach et al., 2009, 2012) using a 13-point box  
1030 averaging algorithm and a 96-point smoothing (black line). Panel C shows AWAP-derived  
1031 monthly PE with a 6-point box smoothing. Panel D shows monthly deep drainage (recharge)  
1032 from AWAP data. Panel E is the annual rainfall from Bureau of Meteorology (Wellington,  
1033 station ID: 065034) with the thick blue line showing the 9-point box smoothing. Panel F  
1034 shows the monthly cumulative rainfall departure (black line) calculated from Bureau of  
1035 Meteorology rainfall data (station ID: 065034); seasonal rainfall departure, where DJF  
1036 represents summer months, MAM represents autumn months, JJA represents winter months  
1037 and SON represents spring months. The period of stalagmite growth for WB (green) and WC  
1038 (orange) are also shown in Panel G at the bottom of the figure.

1039

1040 Figure 3. Upper panel shows cross-section of stalagmite WB (Panel A) and WC (Panel B);  
1041 The sampling transects are indicated in panels C (stalagmite WB) and D (stalagmite WC) and  
1042 the  $\delta^{18}\text{O}$  time series overlain on calcite fabric in panels E (stalagmite WB) and F (stalagmite  
1043 WC). The photographs in the lower panels show a microscope image of the WB flood layer  
1044 (Panel G); the UV fluorescence microscope (365 nm) image of WB microsparite layers at the  
1045 top of the panel before the flood (Panel H); the Ziess microscope image of WB top layers

1046 (Panel I) and microsparite layers below the flood (Panel J); and the surface above Cathedral  
1047 Cave showing the relative positions of 'WB' and 'WC' (Panel K).

1048

1049 Figure 4. Rainfall  $\delta^{18}\text{O}$  versus  $\delta\text{D}$  with the local meteoric waterline (black), precipitation-  
1050 weighted mean annual rainfall (yellow diamond), monthly-integrated rainfall (red stars),  
1051 small volume event rainfall < 5 mm samples (blue triangles) and large volume (> 45mm)  
1052 event rainfall samples (blue circles).

1053

1054 Figure 5. Time series of stalagmite WB  $\delta^{18}\text{O}$  (Panel A) and  $\delta^{13}\text{C}$  (Panel B) and timeseries of  
1055 of WC  $\delta^{18}\text{O}$  (Panel C) and  $\delta^{13}\text{C}$  (Panel D). Scatterplots of stalagmite WB  $\delta^{18}\text{O}$  vs.  $\delta^{13}\text{C}$   
1056 showing  $r^2 = 0.00$  (Panel E) and WC  $\delta^{18}\text{O}$  vs.  $\delta^{13}\text{C}$  (Panel F) showing  $r^2 = 0.77$ . 3-year box-  
1057 smoothing was applied to the time series, shown by the "Trend" (red line). The blue  
1058 background behind each  $\delta^{18}\text{O}_{\text{spel}}$  time series shows the range (-0.13 to -5.53 ‰ VPDB) of  
1059 calculated calcite from the temperature dependent fractionation equation in Kim and O'Neil  
1060 (1997) for the measured drip water values from South Passage from Cuthbert et al. (2014).  
1061  $^{14}\text{C}$  bomb-pulse age and Organic Carbon models presented in Markowska et al. (2019) were  
1062 used to build chronologies for stalagmites WB and WC, respectively.

1063

1064 Figure 6. Coeval  $\delta^{18}\text{O}$  stalagmite records compared to the instrumental record. Panel A shows  
1065 the IOD phases with positive (red rectangles) and negative phases (blue rectangles) (BoM,  
1066 2019a); Panel B shows the positive SOI anomalies (La Niña phases; green) and negative SOI  
1067 anomalies (El Niño phases; yellow) based on the standardised anomaly of the Mean Sea  
1068 Level Pressure difference between Tahiti and Darwin according to the Australian Bureau of  
1069 Meteorology Convention (BoM, 2019); Panel C shows the Monthly Cumulative Rainfall

1070 Deficit (CRD) (thick black line); Winter CRD (blue line); Panel D shows the water excess  
1071 (precipitation (P) – evapotranspiration(ET)) (mm/d) with mean annual P-ET (thick black  
1072 line); Panel E shows WB stalagmite  $\delta^{18}\text{O}$  (red squares) and WC stalagmite  $\delta^{18}\text{O}$  (black  
1073 circles) alongside modelled recharge events (deep drainage (blue), from AWAP). The  
1074 Millennium Drought and WWII Drought are outlined in red and two short droughts (1965-  
1075 1968 CE and 1982-1983 CE) in yellow. Two significant water excess periods are highlighted  
1076 in blue (1950-1952 CE and 1955-1956 CE). Numbers 1-6 correspond to peaks in WC  $\delta^{18}\text{O}_{\text{spel}}$   
1077 (black) and annual water deficits (yellow), respectively.

1078

1079 Figure 7. Conceptual model of Cathedral Cave over wet and dry hydrological periods using  
1080 stalagmites WC and WB as examples. Stalagmite WB is connected to a larger storage  
1081 reservoir than WC, which buffers the response effects of dry periods.

1082

1083 Figure 8. Modelled versus measured  $\delta^{18}\text{O}$  for stalagmites WB and WC. The age model  
1084 uncertainty is delineated by the red error bars for an example sample point.

1085

1086 Figure 9. Model output showing the sensitivity of variables water storage depth below which  
1087 epikarst evaporation occurs, or the volume where epikarst evaporation ‘switches on’ or  
1088 becomes important (S2lim, mm) versus the epikarst evaporation rate (mm/d) and the  
1089 resultant offset in  $\delta^{18}\text{O}$  due to epikarst evaporation. Assuming that our 1D model store  
1090 approximates to the actual 3-dimensional karst void, then the likelihood of discontinuous  
1091 growth is higher when S2lim increases.

Figure 1 revised 191204

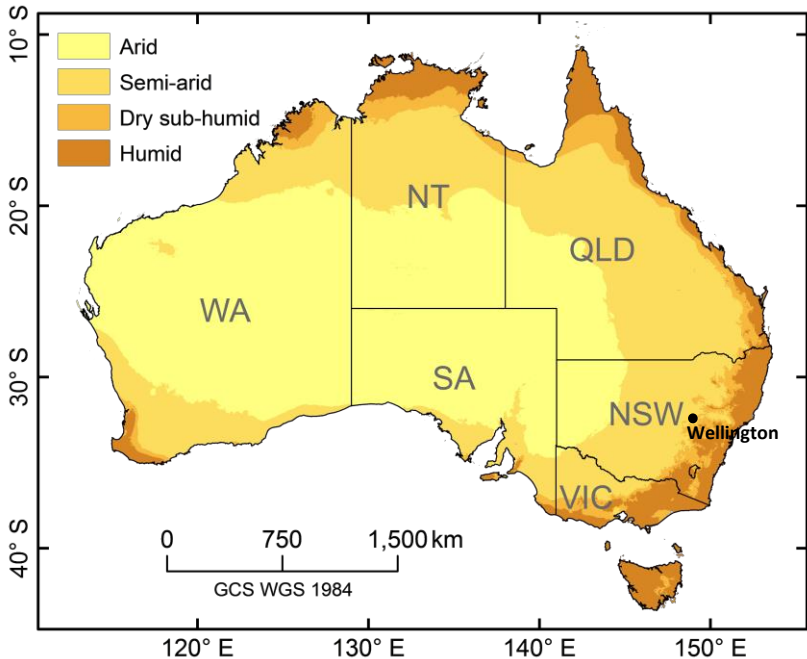
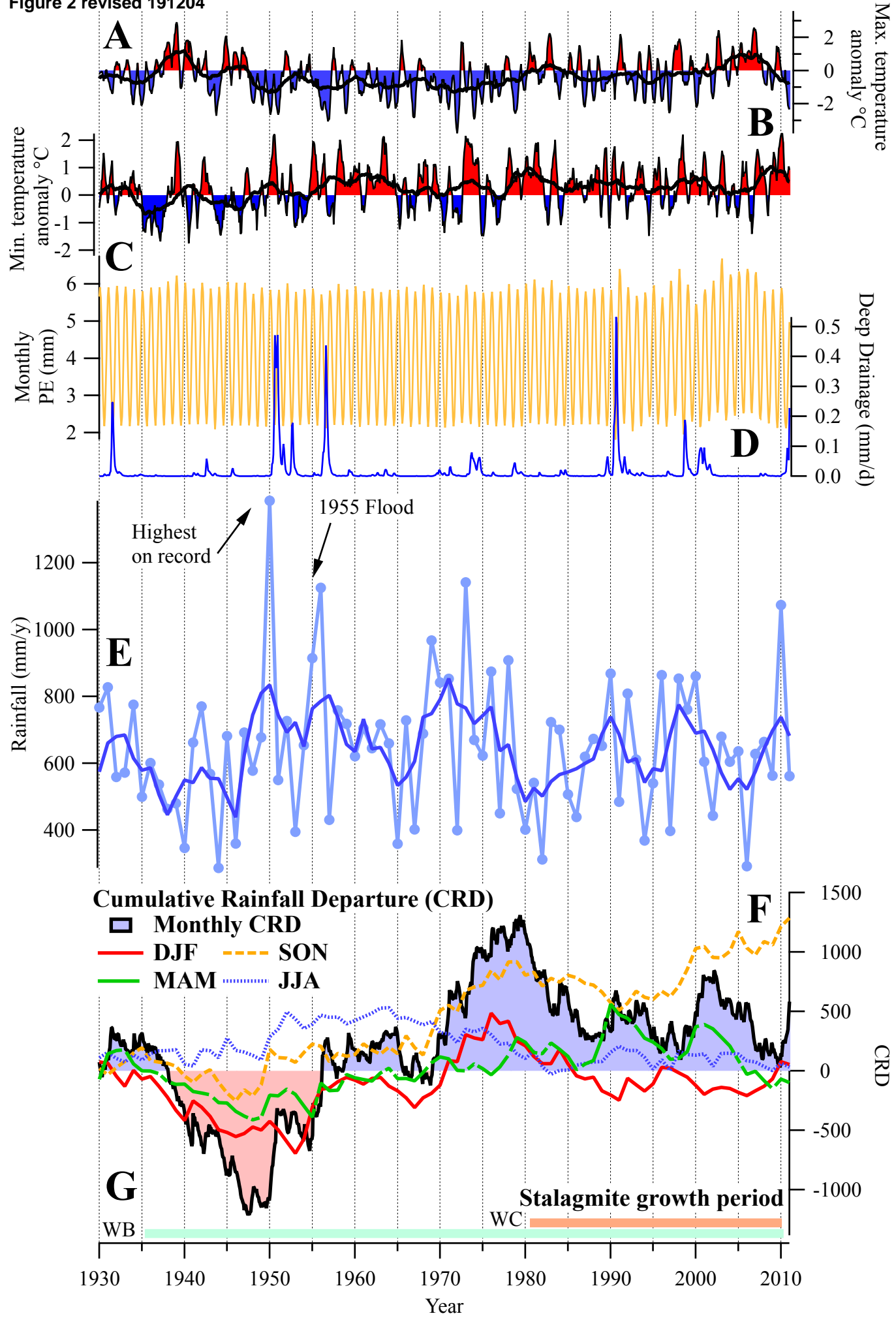


Figure 2 revised 191204



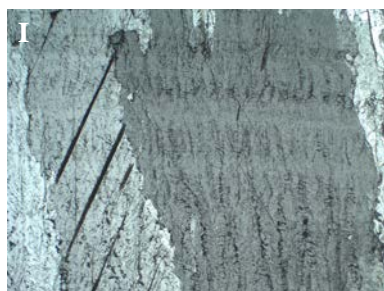
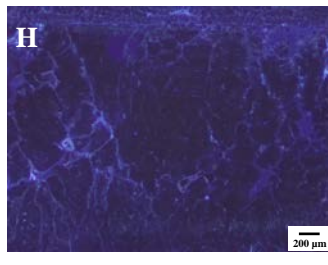
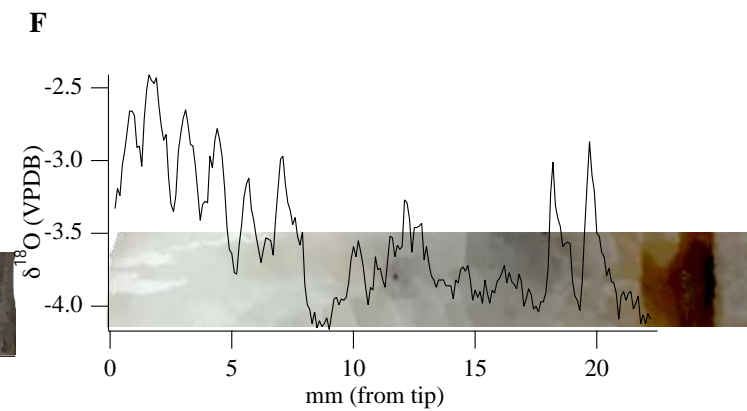
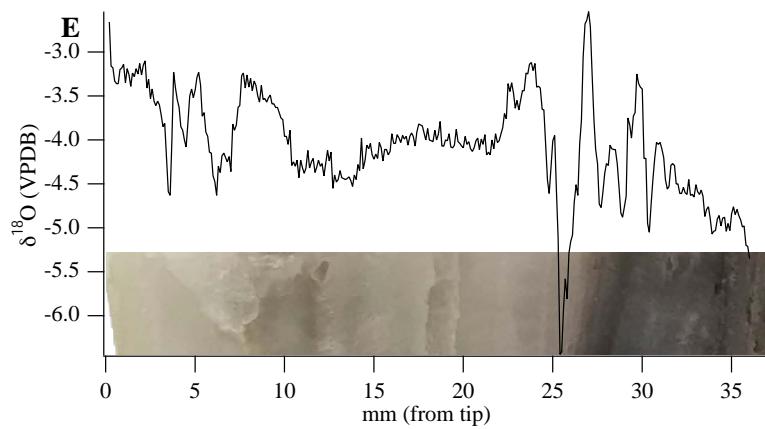
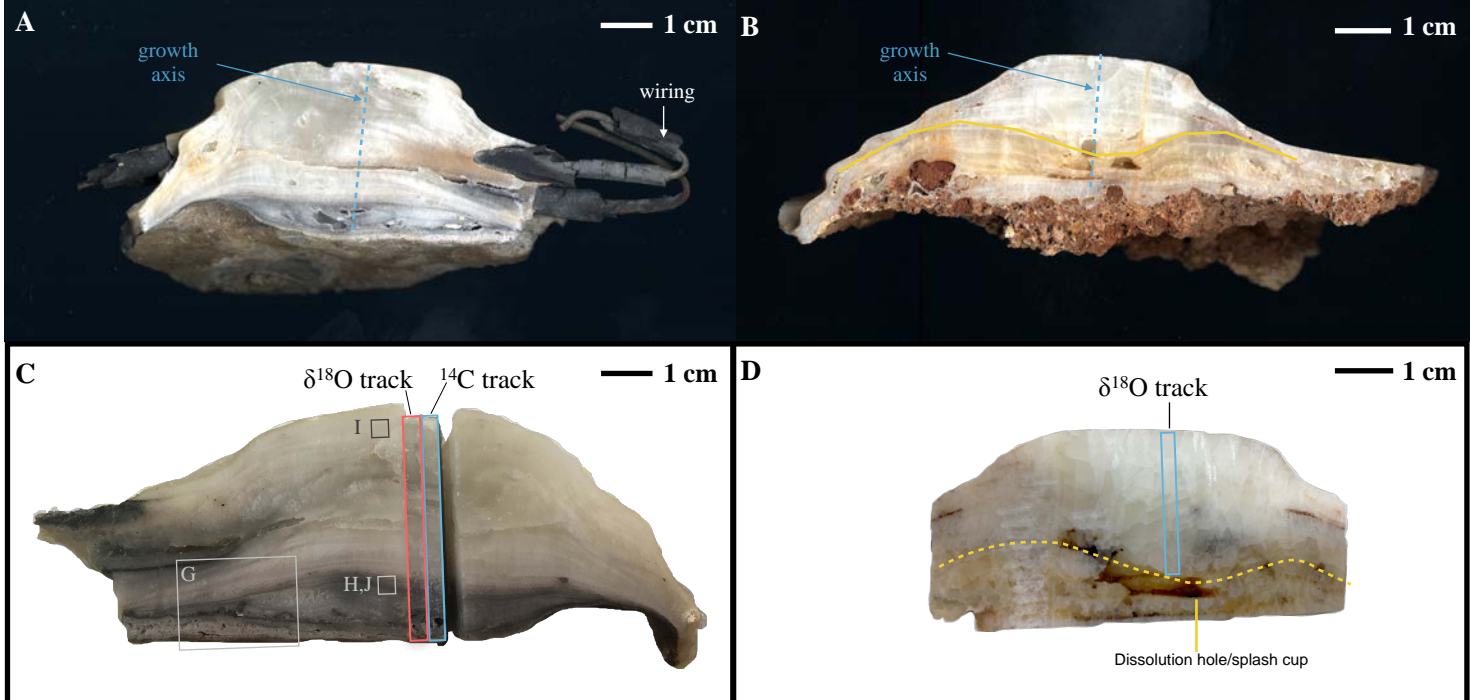
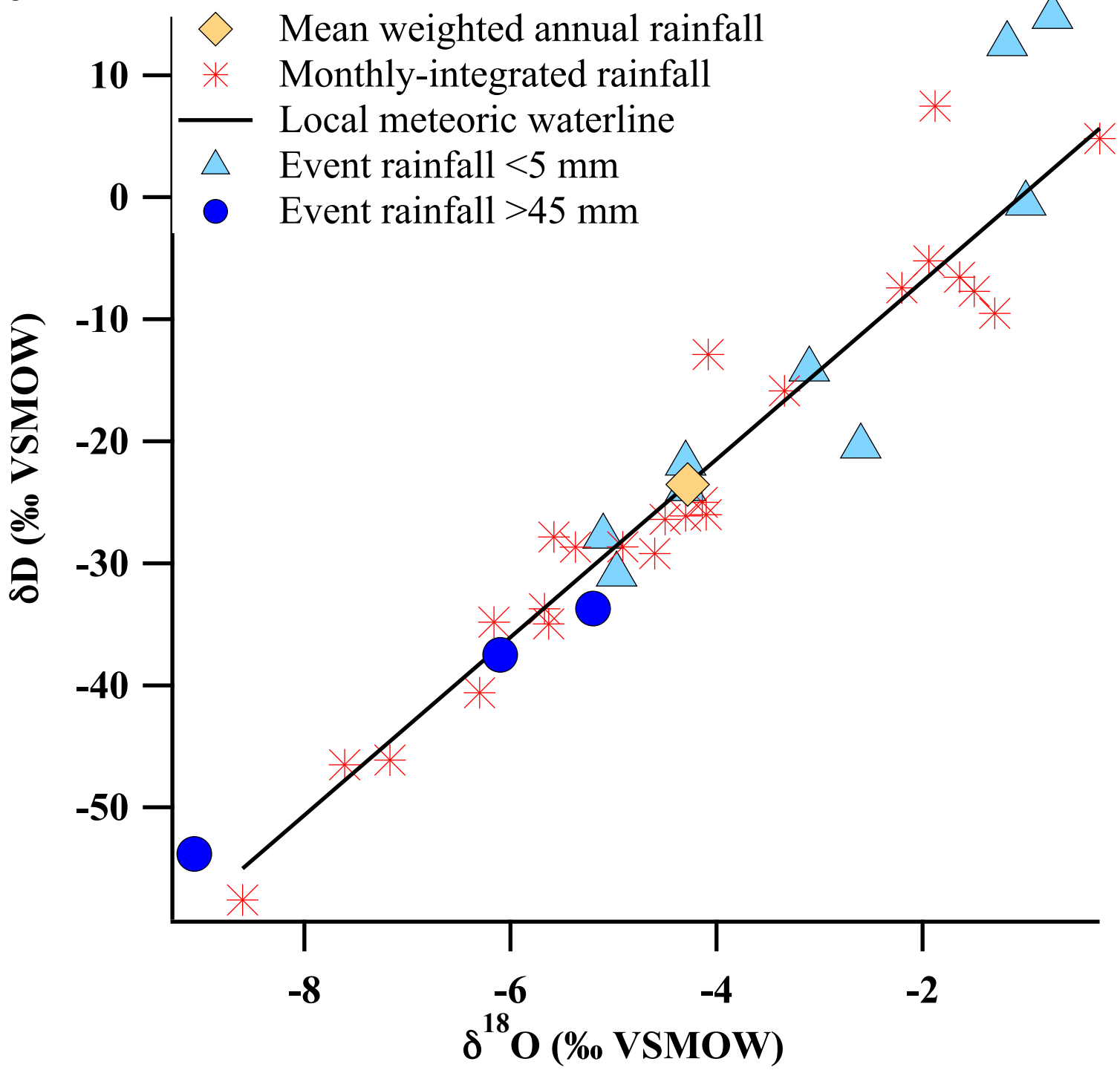




Figure 4



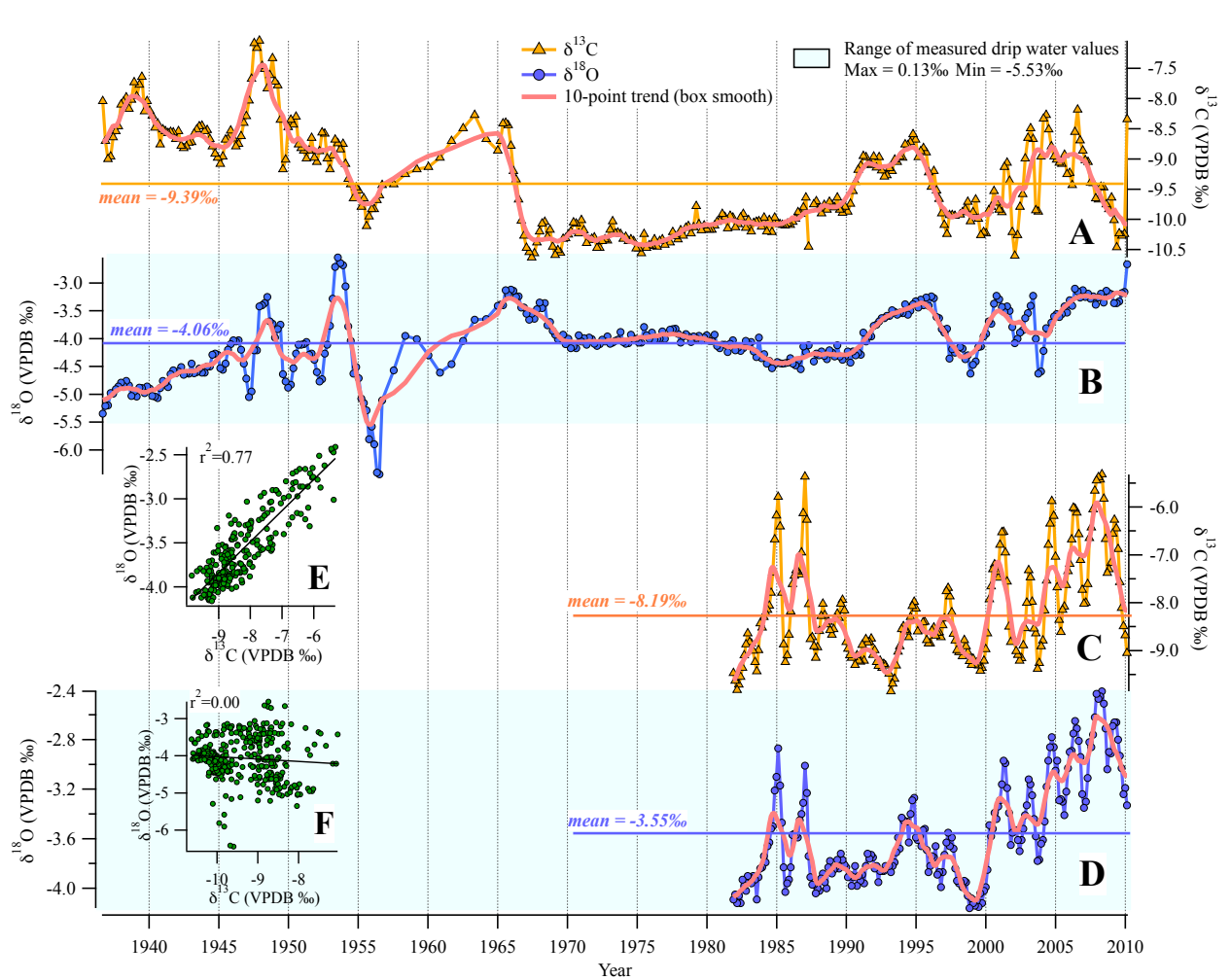
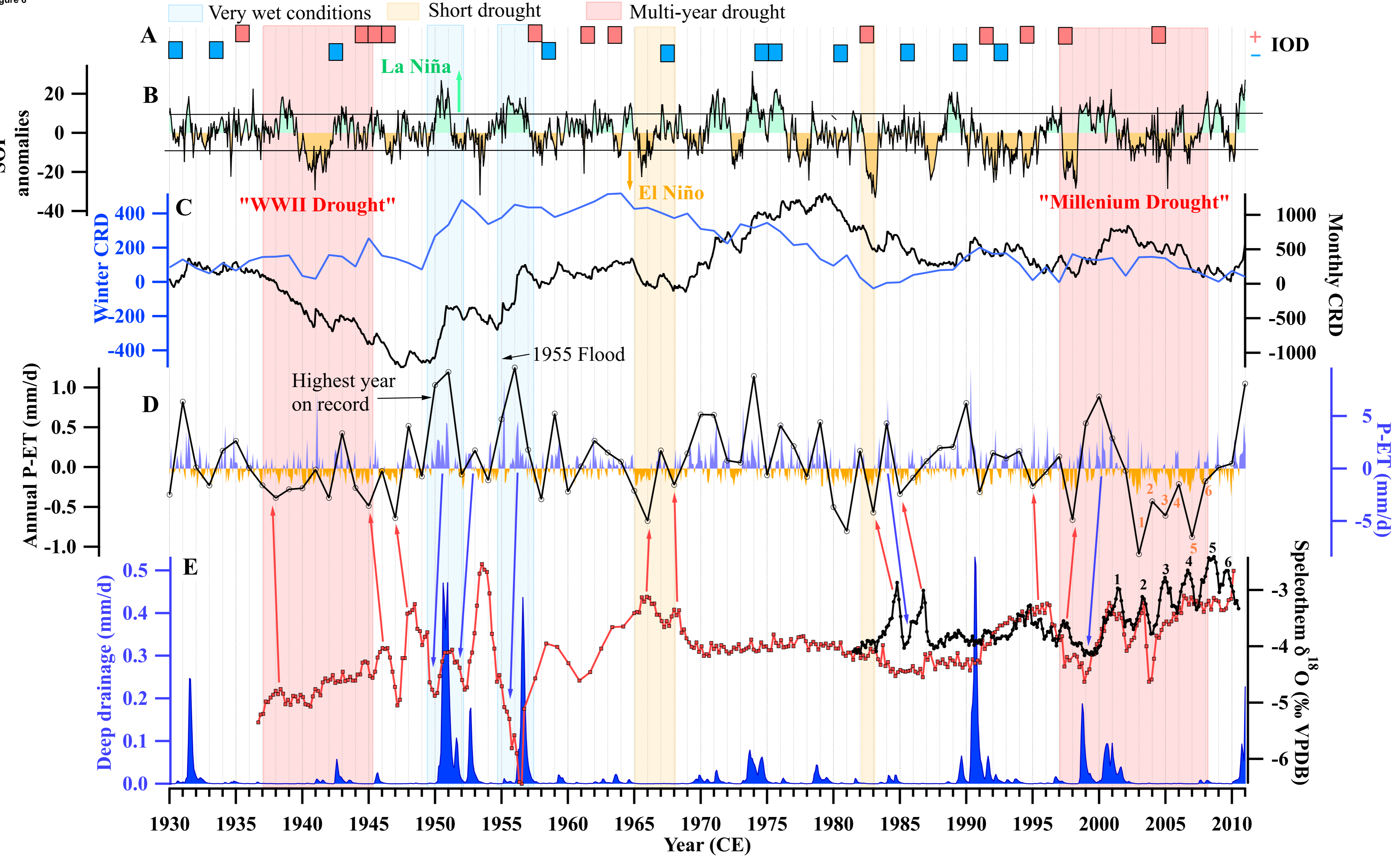


Figure 6



**Controls on speleothem  $\delta^{18}\text{O}$  in drylands caves:  
Example from Cathedral Cave, SE Australia**

**Wet conditions**

**Dry conditions**

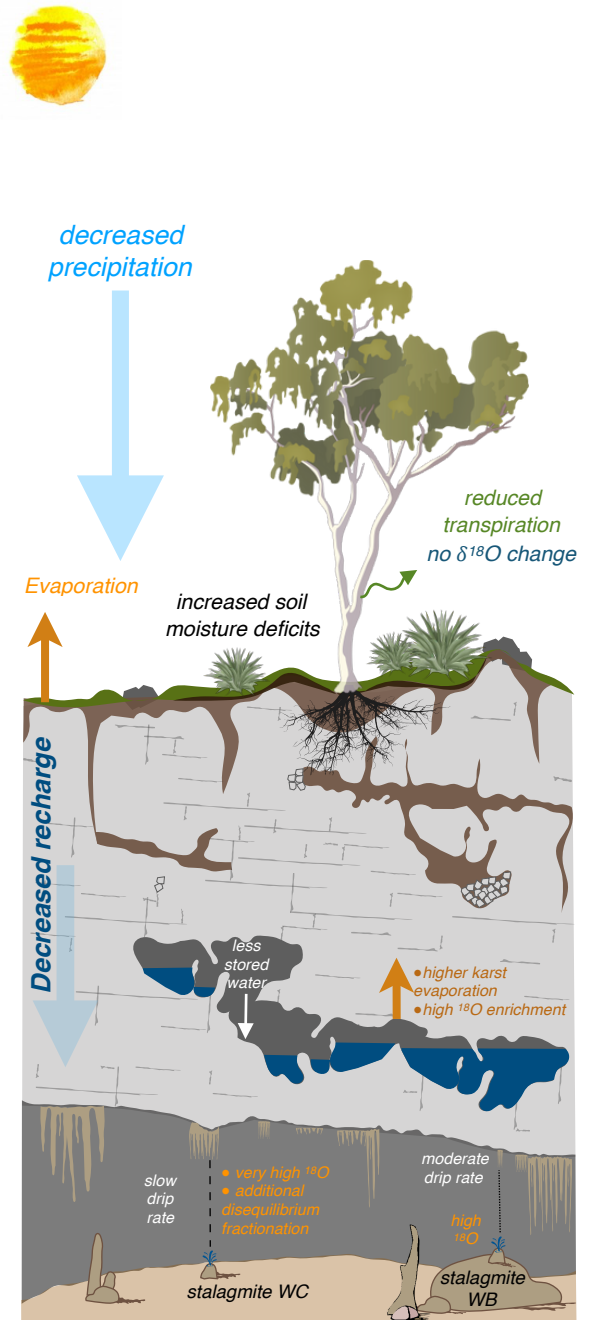
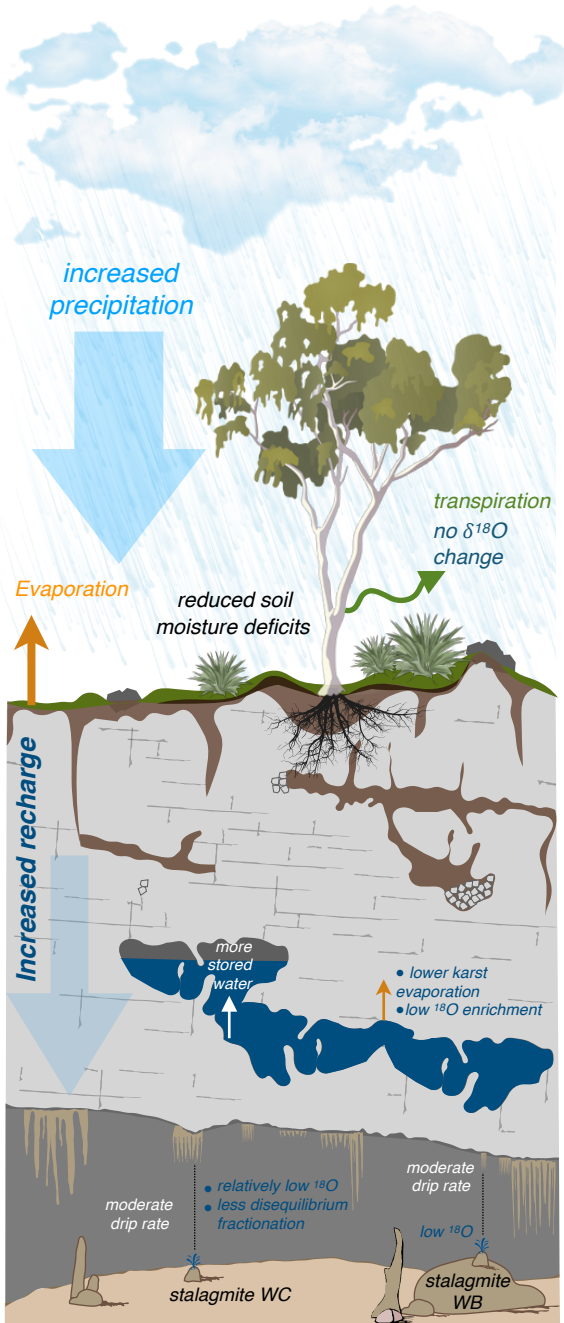
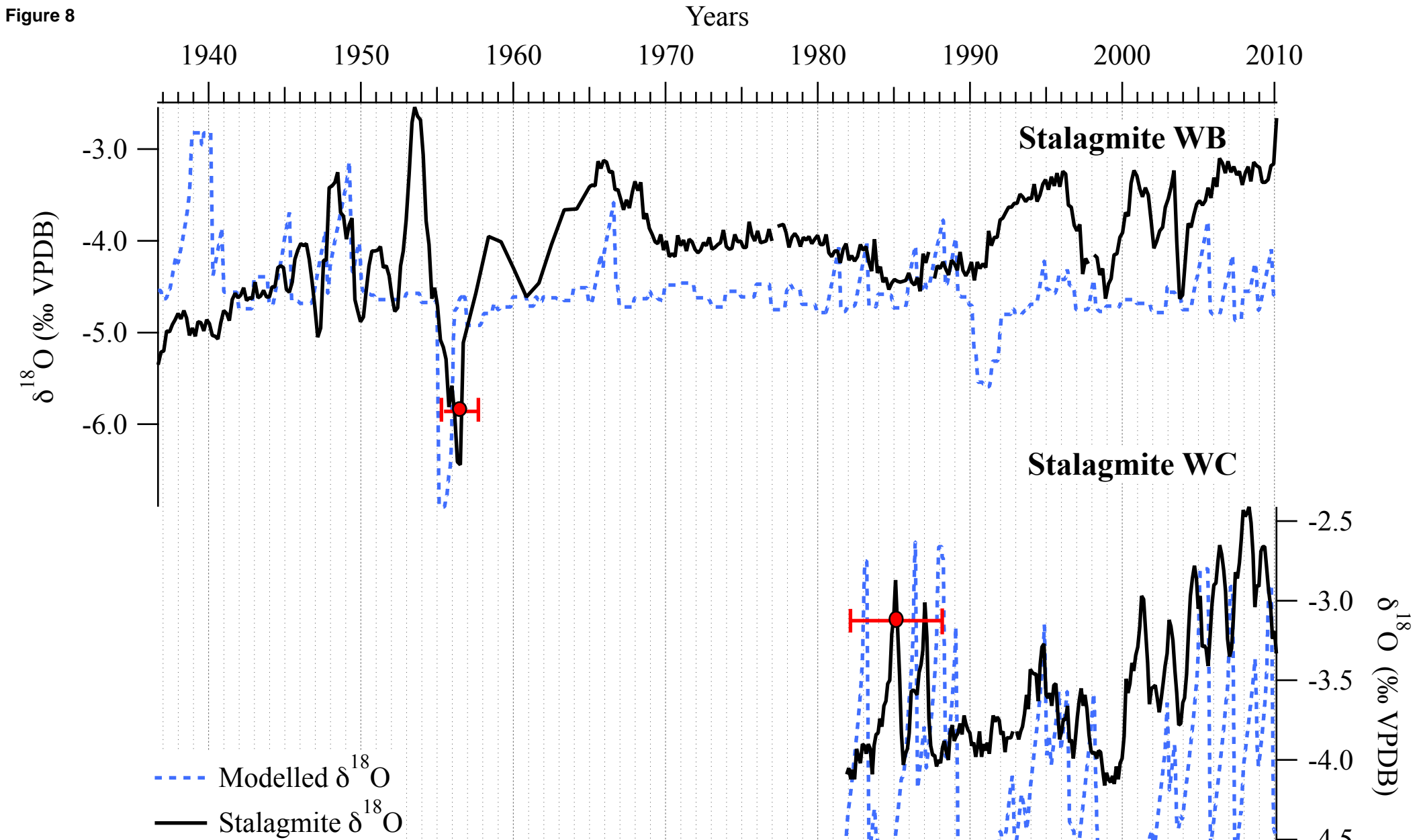
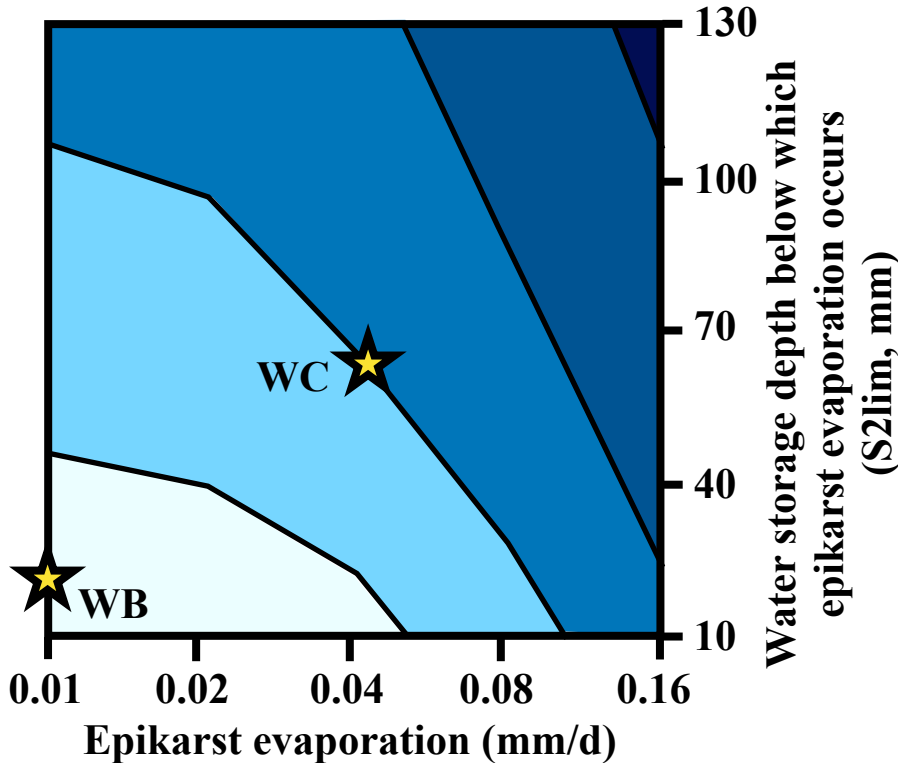
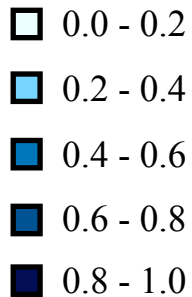


Figure 8



$\delta^{18}\text{O}$  offset  
(‰)



Discontinuous  
growth



Continuous  
growth

## Appendix

[Click here to download Appendix: Appendix - Figure S1 S2 S3.pdf](#)

Source or Other Companion File Example climate input

[Click here to download Source or Other Companion File: Model\\_Climate\\_Input.xlsx](#)



Source or Other Companion File model output calcite conversion

[Click here to download Source or Other Companion File: Calcite conversion.xlsx](#)

**MATLAB File (.fig, .m)**

[Click here to download MATLAB File \(.fig, .m\): Isotope\\_FAO\\_SMBM\\_Markowskaetal\\_GCA2019.m](#)

**Declaration of interests**

The authors declare that they have no known competing financial interests or personal relationships that could have appeared to influence the work reported in this paper.

The authors declare the following financial interests/personal relationships which may be considered as potential competing interests: